High-temperature fracturing and subsequent grain-size-sensitive creep in lower crustal gabbros

AGU PUBLICATIONS

JGR

Journal of Geophysical Research: Solid Earth

RESEARCH ARTICLE
10.1002/2014JB011708

Key Points:
- Shear zones formed by fracturing and subsequent creep are found in gabbro
- Deformation occurred at the lower crustal conditions
- Shear zones are related to a process of coseismic loading followed by creep

Correspondence to:
T. Okudaira,
oku@sci.osaka-cu.ac.jp

Citation:
Okudaira, T., P. Jeřábek, H. Stünitz, and F. Fusseis (2015), High-temperature fracturing and subsequent grain-size-sensitive creep in lower crustal gabbros: Evidence for coseismic loading followed by creep during decaying stress in the lower crust?, *J. Geophys. Res. Solid Earth*, *120*, 3119–3141, doi:10.1002/2014JB011708.

Received 17 OCT 2014
Accepted 8 APR 2015
Accepted article online 22 APR 2015
Published online 26 MAY 2015

High-temperature fracturing and subsequent grain-size-sensitive creep in lower crustal gabbros: Evidence for coseismic loading followed by creep during decaying stress in the lower crust?

Takamoto Okudaira[1], Petr Jeřábek[2], Holger Stünitz[3], and Florian Fusseis[4]

[1]Department of Geosciences, Osaka City University, Osaka, Japan, [2]Institute of Petrology and Structural Geology, Charles University, Prague, Czech Republic, [3]Department of Geology, University of Tromsø, Tromsø, Norway, [4]School of Geosciences, University of Edinburgh, Edinburgh, UK

Abstract The mechanism of shear zone formation in lower crustal, relatively "dry" rocks is still poorly understood. We have studied the high-temperature deformation of the Hasvik gabbro (northern Norway) which commences by fracturing. The 10–20 μm wide fractures show little displacement. The fine-grained plagioclase and orthopyroxene in the fractures lack a crystallographic preferred orientation (CPO) or a systematic crystallographic orientation with respect to the host grains. Fractures grade into narrow shear zones, which are composed of fine (10–20 μm), equant grains of recrystallized plagioclase, amphibole, and pyroxene. Recrystallized plagioclase and pyroxene have compositions different from the magmatic grains, suggesting that they have formed by nucleation and growth. Based on conventional plagioclase-amphibole thermobarometry, the shear zones have formed at temperatures and pressures of 700–750°C and 0.5–0.6 GPa. The observed primary minerals cut by fractures suggest high-temperature fracturing in the absence of high pore pressures, which implies a high strength of the lower crustal gabbros and high stresses at fracturing. The shear zones are characterized by the lack of CPO and a small grain size, suggesting that the mechanism of deformation of the fine-grained plagioclase and orthopyroxene has been grain boundary sliding accommodated by diffusive mass transfer. The amphibole grains have strong CPOs, which most likely result from oriented growth and/or rigid body rotations during deformation. The process that initiated the fracturing and subsequent viscous creep in the Hasvik gabbro may have resulted from a process of coseismic loading followed by creep during decaying stress in the lower crust.

1. Introduction

Gabbros and gabbronorites are major constituents of the lower crust, and they consist mainly of plagioclase, clino- and orthopyroxene, and some amphibole. To evaluate the strength and mechanical behavior of the lower crust, an understanding of the rheological properties and deformation processes of these minerals is crucial. Of particular interest is the process of grain size reduction and potential subsequent grain-size-sensitive deformation, because it is thought to be an important mechanism for shear localization [e.g., *Brodie and Rutter*, 1985; *Rutter*, 1999; *Platt and Behr*, 2011].

Rotation recrystallization is a common grain size reduction mechanism in mafic shear zones under the conditions of upper amphibolite and granulite facies [e.g., *Kruse et al.*, 2001; *Kanagawa et al.*, 2008; *Raimbourg et al.*, 2008], whereas fracturing and/or comminution is the dominant mechanism at lower temperatures, partly because the critical resolved shear stress may not be reached in plagioclase and mafic minerals, and partly because recovery and recrystallization are limited [e.g., *Tullis and Yund*, 1987; *Yund and Tullis*, 1991; *Prior and Wheeler*, 1999].

When the differential stress required to slide on a preexisting fracture/fault is greater than that required to create new fractures, a pervasive (nonlocalized) fracturing of the material occurs, leading to semibrittle deformation [e.g., *Kohlstedt et al.*, 1995; *Tullis and Yund*, 1987; *Pec et al.*, 2012]. The semibrittle deformation involving homogeneously distributed microcracks may occur under high differential stress, nearly equal to mean or confining pressure [i.e., the Goetze criterion; *Kohlstedt et al.*, 1995]. Even under high-temperature conditions where plastic deformation of minerals takes place, fracturing and nucleation of new grains as small fragments have been identified in naturally and experimentally deformed rocks. For feldspar, see for

example, *Tullis and Yund* [1987], *Fitz Gerald and Stünitz* [1993], *Kruse et al.* [2001], *McLaren and Pryer* [2001], *Stünitz et al.* [2003], *Brander et al.* [2012], *Fukuda et al.* [2012], *Fukuda and Okudaira* [2013], and *Menegon et al.* [2013]; for quartz, see *Trepmann and Stöckhert* [2003], *Vernooij et al.* [2006], and *Trepmann et al.* [2007]; for orthopyroxene, see *Raimbourg et al.* [2008]; and for hornblende, see *Imon et al.* [2002, 2004] and *Díaz Aspiroz et al.* [2007]. Particularly for plagioclase and quartz, fracture-related small fragments act as nuclei for new grains, which are characterized by low aspect ratios and weak or absent crystallographic preferred orientation [e.g., *Stünitz et al.*, 2003; *Trepmann et al.*, 2007].

Metamorphic net transfer reactions result in precipitation of fine grains of new phases and dissolution of usually coarse grains of porphyroclasts. Metamorphic crystallization is an important process in shear zone formation. Infiltration of aqueous fluids into shear zones may lead to retrograde hydration reactions [e.g., *Beach*, 1980; *Imon et al.*, 2002; *Wintsch and Yi*, 2002]. Fracturing may facilitate fluid infiltration by promoting increased porosity and permeability [e.g., *Carter et al.*, 1990; *Uehara and Shimamoto*, 2004]. Consequently, fracturing and subsequent fluid infiltration are important processes for the formation of shear zones facilitated by grain size reduction.

Grain-size-sensitive creep is likely to dominate in fine-grained mineral aggregates, as the diffusion paths are short. Grain size is not an equilibrium quantity but rather a property that continuously varies as a result of the competition between grain growth and grain size reducing processes [e.g., *De Bresser et al.*, 2001; *Platt and Behr*, 2011]. In cases where grain-size-sensitive creep dominates deformation on a geological time scale, the recrystallized grain size must be small, and the kinetics of grain growth must be slow. It has been recognized that grain growth is inhibited by the presence of second-phase minerals and impurities that have been segregated to grain boundaries and regions near grain boundaries [e.g., *Stünitz and Fitz Gerald*, 1993; *Skemer and Karato*, 2007]. Fracturing and comminution in a shear zone are likely to result in a mixing of the phases, thus inhibiting grain growth during subsequent annealing and high-*T* deformation. For this reason, polyphase aggregates have a much higher potential to produce and maintain stable grain-size-sensitive creep.

The processes discussed above can be well studied in examples of the Hasvik layered intrusion in northern Norway. The Hasvik gabbro is part of the Late Proterozoic-Middle Cambrian Seiland Igneous Province, which is exposed within the Sørøy-Seiland nappe, the uppermost tectonic unit of the Kalak nappe complex forming the Middle Allochthon of the North Norwegian Caledonides [*Tegner et al.*, 1999] (Figure 1). In minor shear zones in the Hasvik gabbro, there are well-developed microstructures, which are indicative of grain size reduction due to crushing, fracturing, and subsequent grain-size-sensitive creep under high-temperature conditions. The deformation process is inferred to be identical to that of the nonsteady state deformation and annealing experiments [*Trepmann et al.*, 2007], suggesting a process of coseismic loading and subsequent creep during decaying stress in the lower crust. Major earthquakes nucleated in the seismogenic zone can cause faults to propagate well into the underlying lower crustal region at the stage of coseismic displacement [e.g., *Ellis and Stöckhert*, 2004], leading to short-term elevated differential stresses at the tip of a seismically active fault in the lower crust. The high-stress deformation associated with the earthquake may be followed by creep during postseismic stress relaxation involving decreasing strain rates [*Scholz*, 1989]. Microstructures observed in the Hasvik gabbro may be evidence for such episodic loading and subsequent unloading of shear zones, which have initiated during a seismic event.

In this paper, we describe the microstructural and chemical characteristics of shear zones developed in the Hasvik gabbro and discuss the processes leading to deformation of these lower crustal gabbros. We also discuss the mechanical implications of the observed lower crustal deformation process.

2. Geological Setting and Field Occurrence of Shear Zones

The Seiland Igneous Province (SIP) consists of a voluminous suite of plutonic rocks with a wide compositional range including gabbro, peridotite, pyroxenite, syenite, nepheline syenite, and carbonatite [*Robins and Gardner*, 1975]. The alkaline, rift-related, mainly gabbroic rocks were formed at ~570 Ma [*Roberts et al.*, 2006], with a subordinate phase of magmatism at ~530–520 Ma [*Pedersen et al.*, 1989], i.e., long before the emplacement of the Caledonian nappes at ~425–400 Ma [*Dallmeyer et al.*, 1988]. The Hasvik gabbro occupies an area of ~12 km^2 on the southwestern tip of the island of Sørøy in Finnmark. The Hasvik gabbro, previously assigned an age of 700 ± 33 Ma by Sm-Nd mineral/whole-rock isochrons [*Daly et al.*, 1991], yields a U-Pb zircon age of

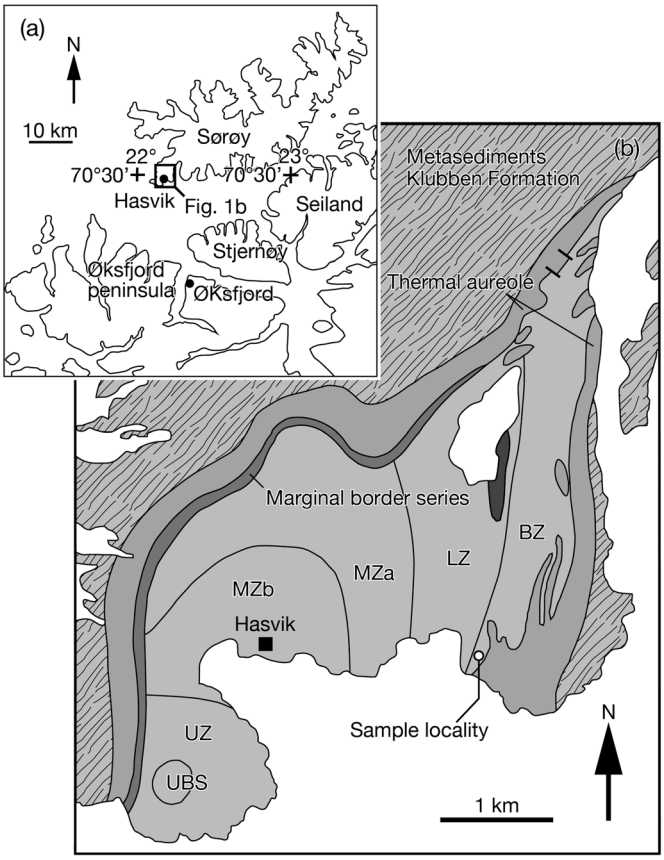

Figure 1. (a) Location map of Sørøya Island, northern Norway. (b) Geological map of the Hasvik gabbro [after *Tegner et al.*, 1999]. UBS = Upper Border Series; UZ = Upper Zone; MZ = Middle Zone; LZ = Lower Zone; and BZ = Basal Zone.

562 ± 6 Ma [*Roberts et al.*, 2006]. *Robins and Gardner* [1975] proposed that the Hasvik gabbro was emplaced in the vertical to overturned limb of a large, preexisting, east verging antiform in the country rocks. In the south, the Hasvik gabbro is a wedge-shaped body, narrowing southward [*Tegner et al.*, 1999]. When followed northward, the almost vertical western contact takes on a steep outward dipping orientation and eventually a moderate northwestward dip where the intrusion pinches out to the north.

The Hasvik gabbro has been subdivided into a narrow Marginal Border Series, a Layered Series, and an Upper Border Series, which have crystallized on the wall, floor, and roof of the magma chamber, respectively [*Tegner et al.*, 1999] (Figure 1). The Layered Series is ~1550 m thick and can be subdivided into four zones defined by distinct cumulus parageneses reflecting the degree of magma differentiation. In stratigraphic order, the zones are as follows [*Tegner et al.*, 1999]: a Basal Zone consisting of laminated gabbronorites (cumulates of plagioclase, orthopyroxene, and augite) with patches of gabbro pegmatite; a Lower Zone consisting of olivine gabbros; a Middle Zone consisting of gabbronorites (MZa in Figure 1) and Fe-Ti oxide gabbronorites (MZb in Figure 1); and an Upper Zone consisting of Fe-Ti oxide-apatite ferronorites. The Hasvik gabbro has a thermal aureole up to 500 m wide with the pressure estimates restricted to 600–750 MPa based on garnet-orthopyroxene-plagioclase-quartz equilibrium and aluminum solubility in orthopyroxene [*Tegner et al.*, 1999, and references therein].

A few millimeter to centimeter wide shear zones and ultramylonites are developed within the Basal Zone of gabbros and gabbronorites (Figure 2), although similar structures were also identified in the Lower and Middle Zones. In the Basal Zone, some shear zones show a narrow fabric transition region to the undeformed rock (Figure 2a); others have a sharp boundary to the undeformed rock and a more crack-like appearance (ultramylonites; Figure 2b). The two types of shear zones can grade into one another (Figure 2c). Some obvious cracks can be associated with the ultramylonites (Figure 2d). These steeply dipping shear zones are sometimes represented by conjugate sets with (i) E-W to ENE-WSW strike and dextral shear sense and (ii) WNW-ESE strike and sinistral shear sense, which together indicate E-W compression. The shear zones can only be followed laterally for a few meters and do not have a regional extent.

We have collected and analyzed several gabbronorite samples from the Basal Zone (Figure 1). Although the microstructural features in all these samples are similar, their chemical characteristics vary due to differences in the bulk rock compositions. To avoid problems with differences in bulk chemical composition between deformed and undeformed material, we only report results of microstructural and chemical analyses of sample SIP II-2 that is from the shear zone in Figure 2d. The thin sections were cut perpendicular to the shear zone and parallel to stretching lineation (*XZ* section of finite strain ellipsoid).

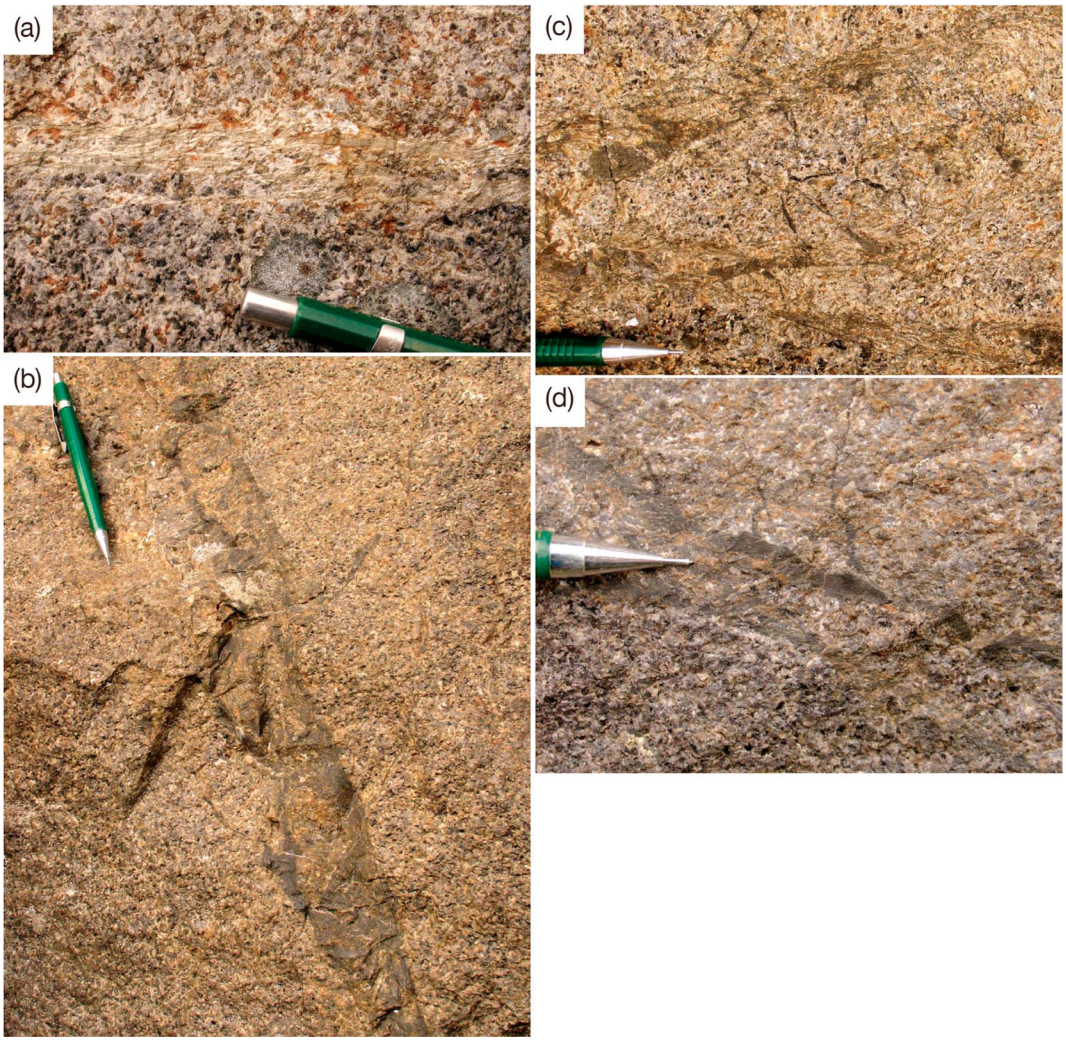

Figure 2. Field images of shear zones in the Hasvik gabbro. (a) Shear zones with steep fabric gradient at shear zone boundary. Some shear zones are very narrow (1 to 2 mm). (b) Dark shear zone without fabric gradient and sharp boundaries. Components in dark matrix can only be resolved in the microscope. (c) Local transitions between the two different types of shear zones. (d) Detail of a dark shear zone with apophysical cracks (i.e., subsidiary mode-I cracks), which are filled with dark matrix material.

3. Methods

For microstructural observations, a light microscope and a scanning electron microscope were used. The grain size of recrystallized minerals was calculated using the image analysis software ImageJ. Grain sizes were calculated as the area equivalent circular diameters of individual grains. For grain size analysis, secondary electron and backscatter electron images were used to manually trace the grain boundaries of individual minerals. Furthermore, to evaluate textures, crystallographic orientations were obtained by means of electron backscatter diffraction (EBSD) technique. The EBSD patterns were obtained using the HKL system (Nordlys detector) attached to the TESCAN VEGA at the Institute of Petrology and Structural Geology, Charles University in Prague, Czech Republic. Working conditions were 20 kV acceleration voltage, 33 mm working distance, ~5 nA beam current, and 70° sample tilt. Pole figures and grain maps were plotted using the MTEX MATLAB toolbox [*Hielscher and Schaeben*, 2008] from the raw electron backscatter diffraction (EBSD) output. The orientation distribution function was calculated by Fourier method, considering de la Vallée Poussin kernel and a half width of 10°. The chemical compositions of the minerals were determined using the CamScan 54 with Link ISIS 300 EDX system at the Institute of Petrology and Structural Geology, Charles University. The analyses were obtained with an accelerating voltage of 15 kV

Table 1. Representative Mineral Chemistry of Constituent Minerals

	Plagioclase			Amphibole		Clinopyroxene		Orthopyroxene		
	Host	Recrystallized		Recrystallized		Host	Recrystallized	Host	Fragment	Recrystallized
		Core	Rim	Core	Rim					
	37/1	39/1	40/1	39-hbl_c	40-hbl_r	36-cpx_c	24-cpx_m	47-opx_c	17-opx_f	3-opx_m
SiO_2	52.17	53.31	55.19	51.31	46.59	51.11	54.12	53.11	52.82	52.35
TiO_2	0.00	0.00	0.00	0.66	1.37	0.69	0.19	0.08	0.55	0.06
Al_2O_3	30.42	29.97	28.05	5.74	9.83	4.68	0.53	2.36	1.21	0.65
FeO	0.26	0.25	0.36	8.76	9.77	6.30	6.15	19.60	21.70	23.08
MnO	0.00	0.00	0.00	0.02	0.10	0.16	0.00	0.48	0.00	0.72
MgO	0.00	0.00	0.00	16.83	14.35	14.01	15.13	24.27	22.90	21.55
CaO	13.26	12.85	10.98	12.49	12.27	22.39	23.98	0.76	0.29	0.39
Na_2O	4.34	4.51	5.60	0.59	1.12	0.44	0.14	0.00	0.00	0.00
K_2O	0.18	0.15	0.21	0.29	0.63	0.00	0.00	0.00	0.00	0.00
Total	100.62	101.04	100.39	96.69	96.04	99.77	100.23	100.66	99.46	98.81
O	8	8	8	23	23	6	6	6	6	6
Si	2.360	2.396	2.486	7.362	6.830	1.890	1.992	1.939	1.966	1.983
Ti	0.000	0.000	0.000	0.071	0.151	0.019	0.005	0.002	0.015	0.002
Al	1.622	1.587	1.489	0.970	1.699	0.204	0.023	0.102	0.053	0.029
Fe	0.010	0.009	0.013	1.051	1.198	0.195	0.189	0.599	0.676	0.731
Mn	0.000	0.000	0.000	0.003	0.013	0.005	0.000	0.015	0.000	0.023
Mg	0.000	0.000	0.000	3.598	3.135	0.772	0.830	1.321	1.270	1.217
Ca	0.643	0.618	0.530	1.920	1.926	0.887	0.946	0.030	0.011	0.016
Na	0.380	0.393	0.489	0.164	0.319	0.032	0.010	0.000	0.000	0.000
K	0.010	0.009	0.012	0.053	0.118	0.000	0.000	0.000	0.000	0.000
Total	5.024	5.012	5.019	15.191	15.389	4.004	3.996	4.007	3.992	4.001
X_{An}[a]	0.62	0.61	0.51							
X_{Mg}[b]				0.80	0.78	0.81	0.81	0.70	0.65	0.63
X_{Wo}[c]						0.48	0.48	0.02	0.01	0.01
^{iv}Al[d]				0.67	1.22					
A-site[d]				0.14	0.28					

[a] $X_{An} = Ca/(Ca + Na + K)$.
[b] $X_{Mg} = Mg/(Mg + Fe^{2+})$.
[c] $X_{Wo} = Ca/(Ca + Mg + Fe^{2+})$.
[d] The structural formula of amphibole is obtained by an average of the maximum (15eK) and minimum (15eNK) estimated of ferric iron [*Leake et al.*, 1997].

and a beam current of 1.5 nA from a circular region of ~2 μm in diameter. Representative mineral chemistry of constituent minerals is listed in Table 1. Mineral abbreviations used here are after *Kretz* [1983].

We collected high-resolution synchrotron X-radiation microtomography data at beamline 2-BM at the Advanced Photon Source, Argonne National Laboratory, Chicago. A Si(111) monochromator provided 27 keV X-rays; images were collected in transmission mode by a charge-coupled device camera positioned behind the sample in the hutch configuration. Data were collected through rotating the samples in 0.25° steps over 180°. The minimum effective pixel size achieved was 1.3 μm to give 2.197 μm^3 voxels for three-dimensional rendering of volumes. Samples of approximately $3 \times 3 \times 5$ mm were cut from the same chip, from which the thin section was made. The X-ray attenuations of plagioclase, pyroxene, amphibole, and pores are sufficiently different to segment the individual phases in the microtomographic data.

4. Results

4.1. Microstructures

On a microscopic scale, there are many intragranular and intergranular fractures, which cut across the magmatic plagioclase and pyroxene grains (Figures 3 and 4b). Shear offsets typically are very small (maximum of a couple of hundred microns). Some pyroxene and plagioclase grains are bent, and twin and cleavage planes tend to be parallel to the fractures. The density of deformation twins and undulatory extinction in plagioclase tends to be higher in regions adjacent to fractures. Most twins are tapered and bent and often do not terminate at grain boundaries, indicating their origin through deformation. Pyroxene porphyroclasts are characterized by the presence of exsolution lamellae, clinopyroxene lamellae

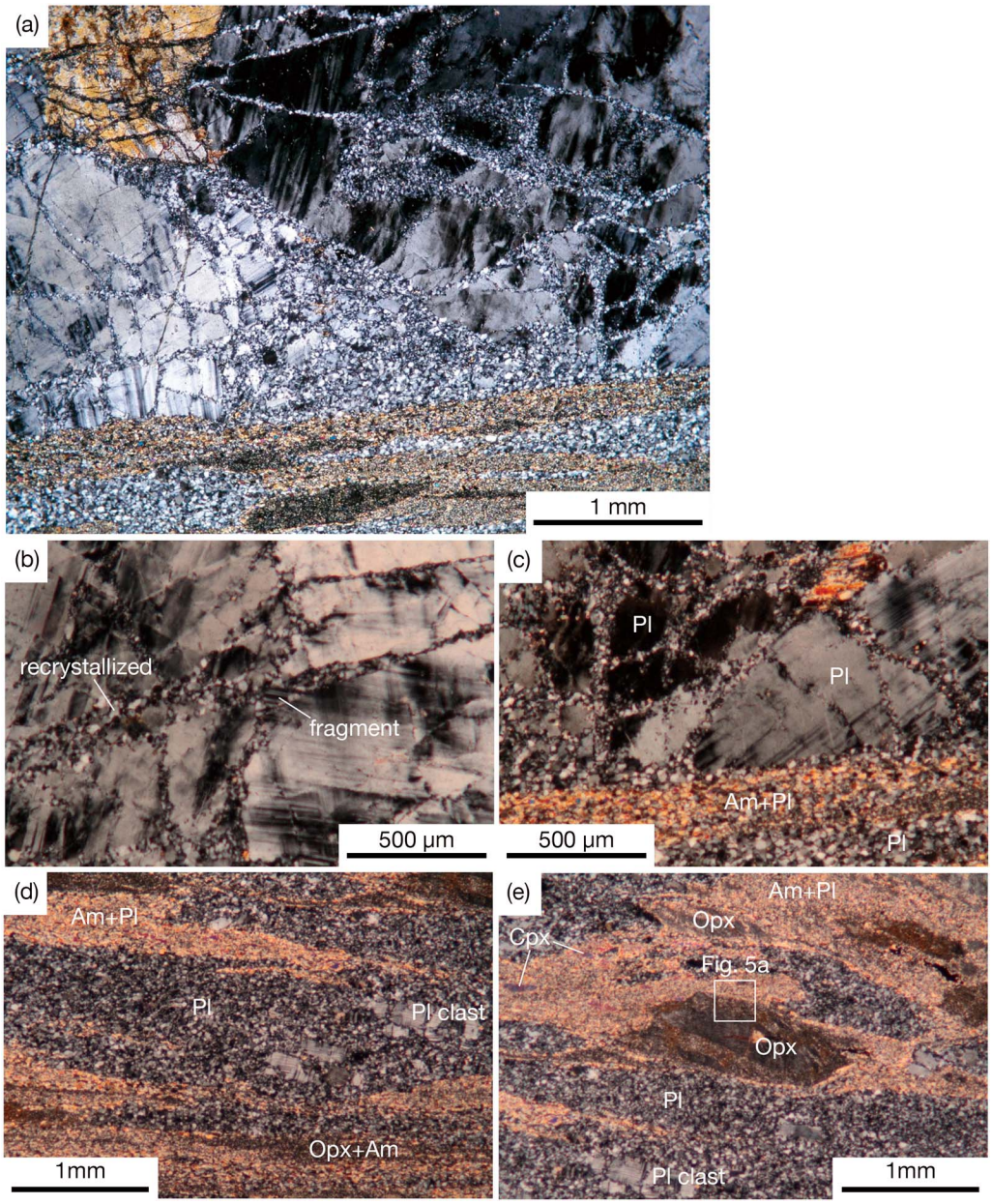

Figure 3. Light micrographs showing deformation microstructures. (a) Overview of ultramylonite shear zone (bottom) and associated cracks, which are oriented at a low angle to the ultramylonite zone (above). Crossed-polarized light. (b) Intragranular and intergranular fractures in plagioclase in the host rock. Crossed-polarized light. (c) Boundary between the fractured host rock and the shear zone. Crossed-polarized light. (d) Compositional banding with alternating polyphase plagioclase-amphibole layers, pyroxene-amphibole layers, and near-monophase plagioclase layers. Porphyroclasts of plagioclase and of clinopyroxene and orthopyroxene are found within the near-monophase plagioclase layers and within the pyroxene-amphibole layers, respectively. Crossed-polarized light. (e) Asymmetric tails of a mixture of orthopyroxene + amphibole developed around an orthopyroxene porphyroclast. In the orthopyroxene + amphibole layers, tiny clinopyroxene clasts are also found (see Figure 5a). At the margins of the mixture, the mixture is made up of amphibole + plagioclase. Crossed-polarized light.

within the orthopyroxene porphyroclasts, and vice versa. Furthermore, both pyroxenes contain frequent rutile exsolution needles oriented parallel to pyroxene lamellae.

The fractures are often filled by recrystallized small grains of plagioclase, amphibole, and pyroxene (Figures 3a–3c). Fractures crosscutting plagioclase porphyroclasts are dominated by plagioclase grains,

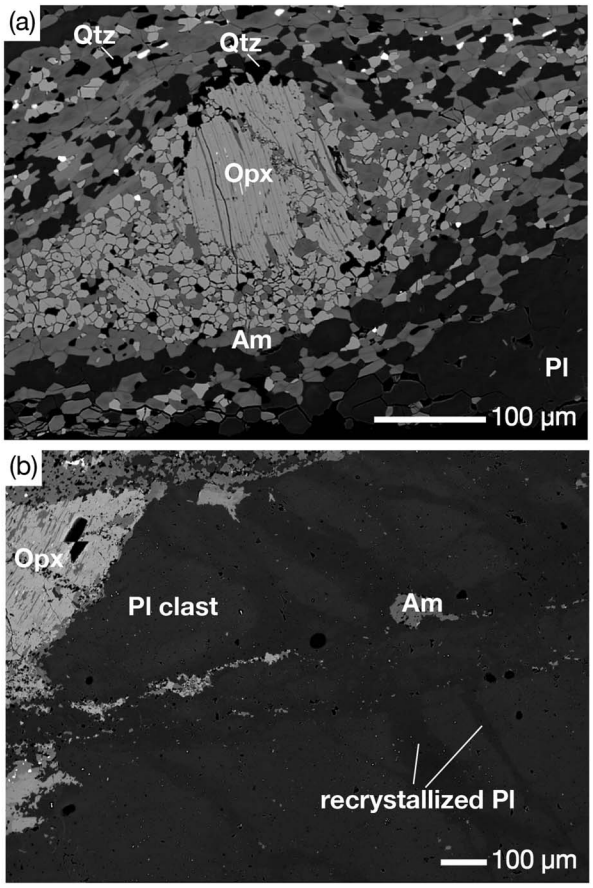

Figure 4. Backscatter electron (BSE) images showing characteristic microstructures. (a) BSE image of microstructure representing the development of tails of the mixture of recrystallized orthopyroxene and amphibole around an orthopyroxene porphyroclast. Quartz grains (black) are found with the amphibole grains. Amphibole grains exhibit compositional zoning, darker cores, and lighter rims. (b) BSE image of intragranular shear zones mainly constituted by fine-grained, recrystallized plagioclase grains within a plagioclase porphyroclast. Chemical compositions of the recrystallized plagioclase differ from those of the host porphyroclast (lighter).

while fractures crosscutting pyroxenes are dominated by mixture of pyroxene-amphibole matrix. The grains in fractures of orthopyroxene and plagioclase typically are rounded, and their orientations are different from those of the host grains. These particular structures possibly result from the brittle fracturing and rotation of the fragments in the course of displacement along the shear fractures. Subsequent or during the rotation, fragmented grains have been dissolved and/or grown (recrystallized grains), because they all show a narrow grain size range.

In the vicinity of fractures, the pyroxene porphyroclasts are partly replaced by amphibole along cleavage planes (Figure 4). The shapes of the recrystallized plagioclase tend to be isometric or slightly elongated and oblique to the fracture (Figures 3b and 3c). The recrystallized grains usually are not twinned (probably because the stresses were not high enough to twin the small grains), so they can easily be distinguished from larger twinned porphyroclast fragments. The narrower the fracture zone is, the smaller the recrystallized grain size of plagioclase appears to be.

At the boundaries between magmatic plagioclase and pyroxenes in the host rock, the development of metamorphic amphibole is limited, whereas the intragranular fractures within pyroxenes are composed mainly of the recrystallized pyroxene and amphibole grains characterized by isometric shapes. Furthermore, the recrystallized pyroxene-amphibole matrix contains rounded grains of ilmenite, while the rutile needles disappear.

Relatively thick ultramylonites are made of a matrix of fine-grained plagioclase and amphibole surrounding pyroxene and plagioclase porphyroclast relics (Figures 3a, 3d, and 3e). The boundaries between the shear zone and the fractured host rock are usually sharp, i.e., lacking a strain gradient toward the host rock (Figures 3a and 3c). Most fractures make a low angle to the shear zones or are parallel to it. They never cut the shear zones, so that there is always a clear sequence of first, fracture formation, and then viscous shear deformation of the shear zones and ultramylonites.

In the ultramylonites, the plagioclase and pyroxenes can be roughly divided into three microstructurally distinct subsets: large inherited porphyroclasts, recrystallized small grains along the rim and within the porphyroclasts, and the fine-grained matrix minerals in the shear zone. The large pyroxene porphyroclasts are usually fragmented into smaller clasts, which are separated by zones of mixed pyroxene-amphibole grains with variable thickness.

Porphyroclasts of pyroxene have tails of recrystallized fine-grained amphibole-pyroxene mixtures and amphibole aggregates. The tails, which extend from orthopyroxene porphyroclasts, are dominated by recrystallized orthopyroxene (with some amphibole; Figure 4a), while the tails from clinopyroxene porphyroclasts show an equal proportion of clinopyroxene and amphibole grains. With increasing distance from pyroxene

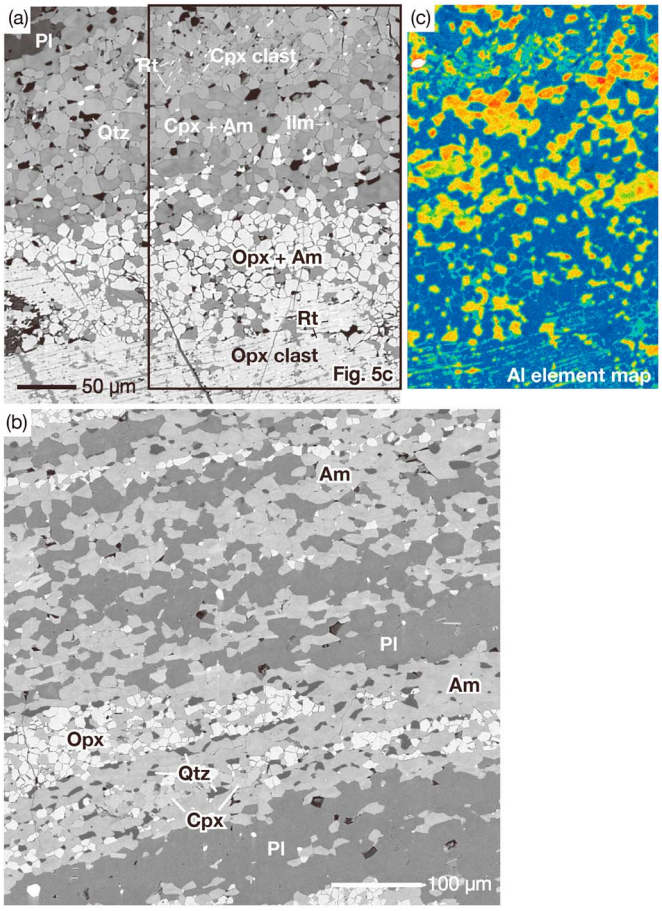

Figure 5. Backscatter electron (BSE) and element X-ray images showing characteristic microstructures. (a) BSE image of mixtures with different mineral assemblages in the shear zone between orthopyroxene and clinopyroxene, i.e., an orthopyroxene-amphibole mixture near the orthopyroxene porphyroclast and a clinopyroxene-amphibole mixture near the clinopyroxene porphyroclast. Rutile (bright) lamellae are found in the host grains but not in the recrystallized grains. In the matrix, ilmenite is ubiquitous, but not rutile. Quartz grains (black) are found in the mixture. Compositional zoning is found within some amphiboles, where certain grains have darker cores than rims, and vice versa. (b) BSE image showing compositional banding with alternating polyphase plagioclase-amphibole, pyroxene-amphibole, and near-monophase plagioclase layers. Quartz grains are frequently observed in pyroxene-amphibole layers. Estimation of the effective bulk-rock compositions was also used as the result from the entire scan of this area. (c) X-ray mapping image for aluminum of the area indicated in Figure 5a. There is a difference in the composition between amphibole grains in different layers; the aluminum contents in amphibole grains in the vicinity of clinopyroxene are higher than those close to orthopyroxene.

porphyroclasts, the proportion of amphibole increases and locally near-monophase amphibole aggregates occur. These microstructures indicate a progressive metamorphic transformation together with deformation. The recrystallized grains of plagioclase and pyroxenes and newly formed amphibole are mixed immediately adjacent to the porphyroclasts (Figures 3e, 4a, and 5a), indicating that the mixing is primarily a result of the reaction in combination with deformation. The recrystallized clinopyroxene is less abundant than orthopyroxene in the shear zones. There is a compositional banding with alternating polyphase plagioclase-amphibole layers, pyroxene-amphibole layers, and near-monophase plagioclase layers (Figures 3d, 3e, 5a, and 5b), suggesting that once the mixture of recrystallized grains has formed, it is maintained during progressive deformation. These layered zones form a thinly laminated ultramylonite structure. Porphyroclasts of plagioclase are found within the layers of near-monophase aggregate of plagioclase and clinopyroxene/orthopyroxene clasts in the mixture of pyroxene-amphibole (Figures 4a and 5a). Quartz grains are often found in the polyphase layers typically in the vicinity of pyroxene grains (Figures 4a and 5b). Fine-grained biotite is occa-sionally found in the ultramylonites, and their cleavage is aligned parallel to the shear plane, suggesting that they crystallized at the time of formation of the ultramylonites.

The recrystallized grain size of plagioclase in the monophase layers ranges from ~10 to 25 μm (Figure 6a), and the aspect ratio is ~1.6. In the polyphase layers, the grain size of plagioclase is smaller (<~15 μm). The grain size of the recrystallized amphibole in the shear zones ranges from ~5 to 15 μm (Figure 6b), and the aspect ratio is ~1.7. The averaged grain size of the recrystallized pyroxenes is ~7 μm (Figures 6c and 6d), and their aspect ratio is ~1.6. The long axes of the recrystallized minerals tend to be aligned parallel to stretching direction of the shear zones, leading to a weak shape preferred orientation.

The recrystallized grains lack a crystallographic preferred orientation (CPO) and a systematic crystallographic orientation relationship with respect to the host grains (Figure 7). Two large grains on both side of the fracture zone have a similar orientation, showing that they were a single crystal before being separated by

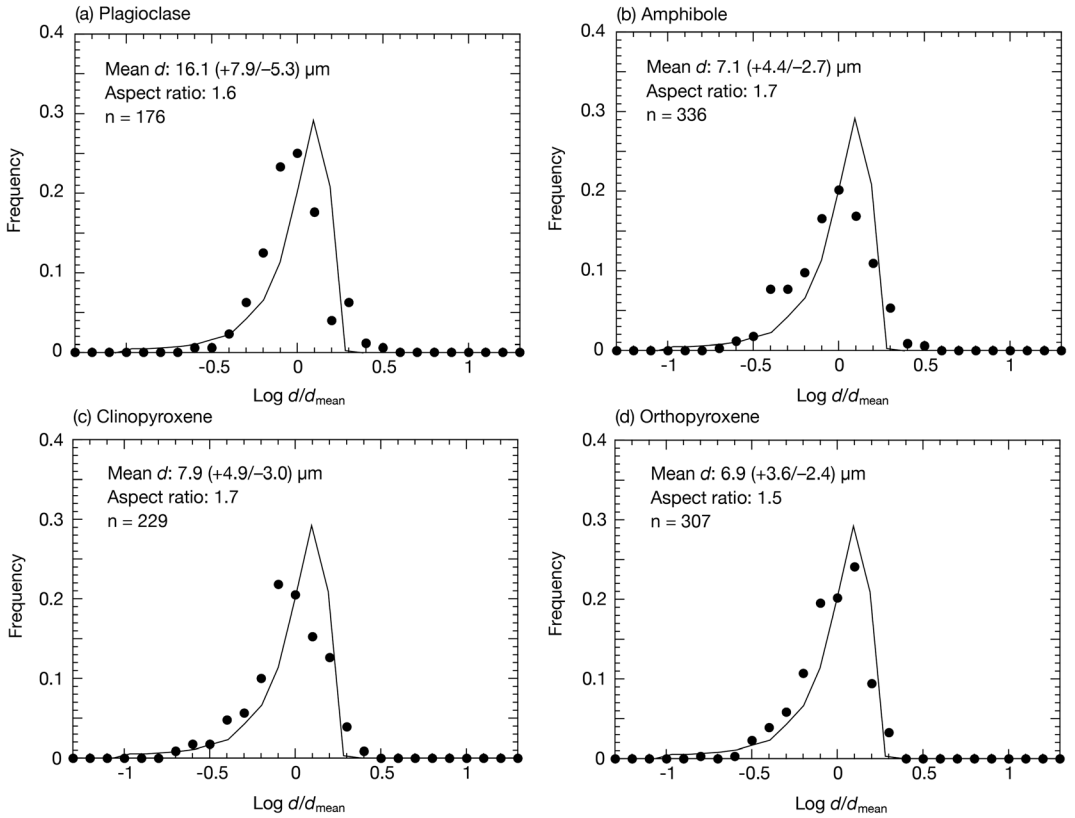

Figure 6. Frequency versus logarithmic normalized grain size (d/d_{mean}) plot. (a) Plagioclase. (b) Amphibole. (c) Clinopyroxene. (d) Orthopyroxene. The solid line represents the theoretical Lifshitz-Slyosov-Wagner distribution in two dimensions for spherical crystals [*Miyazaki*, 1991].

the fracture zone (Figure 7a). The fragmented porphyroclasts show only a small variation in crystallographic orientation (typically less than ~5°; Figure 7a). High-angle boundaries are common between porphyroclast and recrystallized grains at rims of porphyroclast (for plagioclase and orthopyroxene; Figures 7a and 7b). The crystallographic axes of the recrystallized grains are scattered over the whole pole figure. There is no systematic crystallographic relationship to the recrystallized grains and the host porphyroclasts, and there is no common rotation axis for them. The metamorphic amphibole grains in the fracture zones within pyroxene porphyroclasts have the similar crystallographic orientation to the host pyroxenes, and they mimic the pyroxene lattice symmetry.

The CPOs for the recrystallized grains of plagioclase in the monophase plagioclase layer and orthopyroxene and amphibole grains in the layer of orthopyroxene-amphibole mixture are shown in Figure 8. The pole figures show that the recrystallized plagioclase layer has a random or a faint CPO with poles to (001) normal to foliation and with [100] axes aligned normal to lineation. Orthopyroxene grains show weak CPOs with poles to (100) normal to foliation and with [001] axes aligned parallel to lineation. This CPO pattern is not consistent with the dominant slip systems (100)[001] and (010)[001] in naturally and experimentally deformed orthopyroxene [e.g., *Kohlstedt and Vander Sande*, 1973; *Ross and Nielsen*, 1978; *Steuten and van Roermund*, 1989; *Raimbourg et al.*, 2008]. There is a strong amphibole CPO with (100) normal to foliation and [001] parallel to lineation.

4.2. Mineral Chemistry

Magmatic porphyroclasts of plagioclase generally have higher anorthite contents than the recrystallized grains (Figures 4b and 9). The cores of recrystallized grains occasionally have anorthite contents close to those of the magmatic porphyroclasts (especially in fractures; Figure 4b), while the rims have lower contents. Plagioclase inclusions within clinopyroxene porphyroclasts have extremely high anorthite contents (Figure 9). Systematic chemical variations at the margins of plagioclase porphyroclasts were not observed.

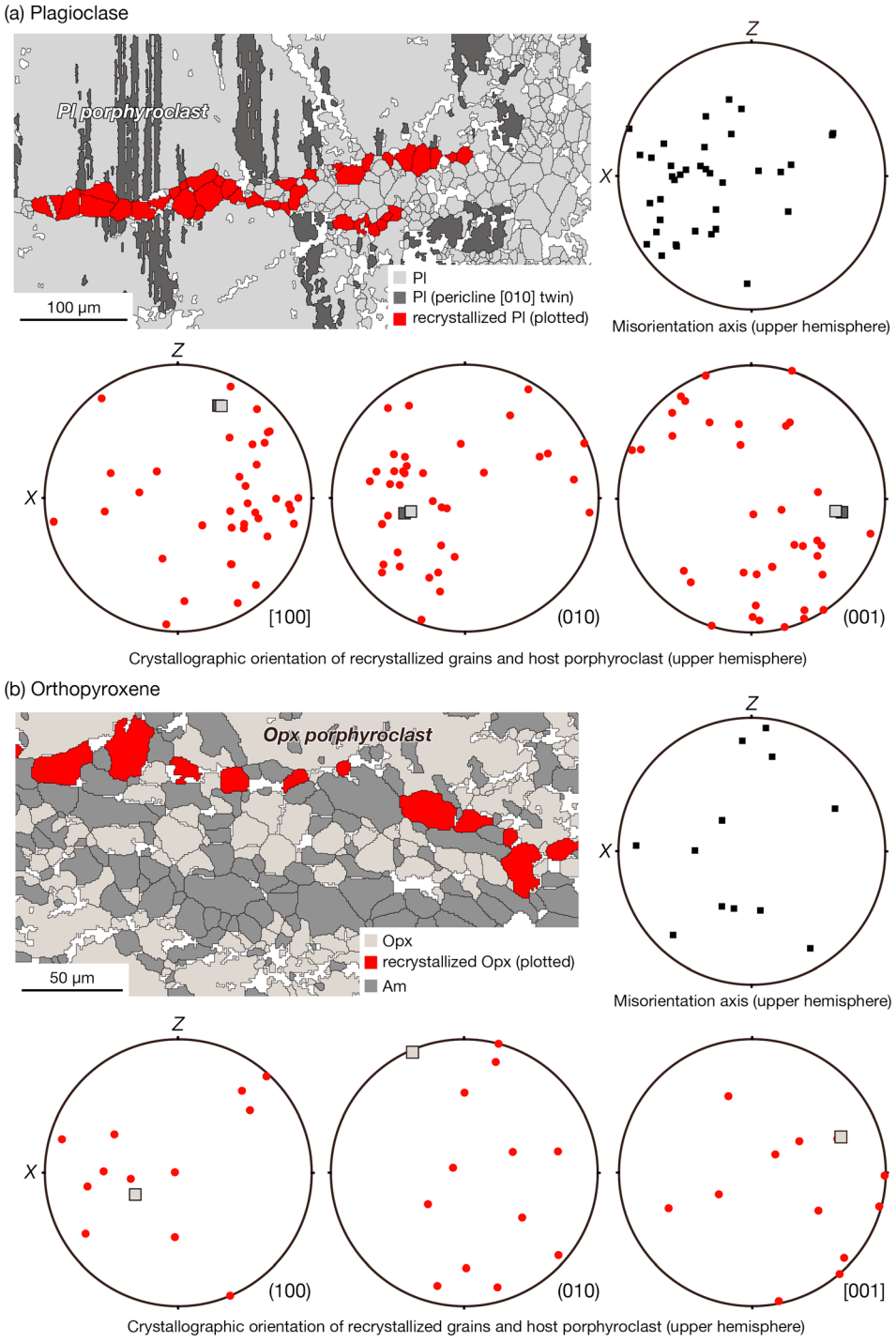

Figure 7. Crystallographic relationship between the recrystallized grains and the host porphyroclast of plagioclase and of orthopyroxene. (a) Grain map is for a region of fracture zone within plagioclase porphyroclast, showing the recrystallized grains plotted here. Pole figures (equal-area, upper-hemisphere stereographic projections in the strain reference frame, with the foliation (*XY* plane) vertical and striking E-W, and lineation (*X* direction) horizontal, trending E-W) are of poles to (010) and (001) planes, and [100] axes of the host grain and the recrystallized grains. Distribution of misorientation axis between the recrystallized grains and the host porphyroclast is also presented. (b) The grain map is for a region of fracture zone within orthopyroxene porphyroclast, showing the plotted recrystallized grains. Pole figures are of poles to (100) and (010) planes, and [001] axes of the host grain and the recrystallized grains for orthopyroxene. Distribution of misorientation axis between the recrystallized grains and the host porphyroclast is also shown.

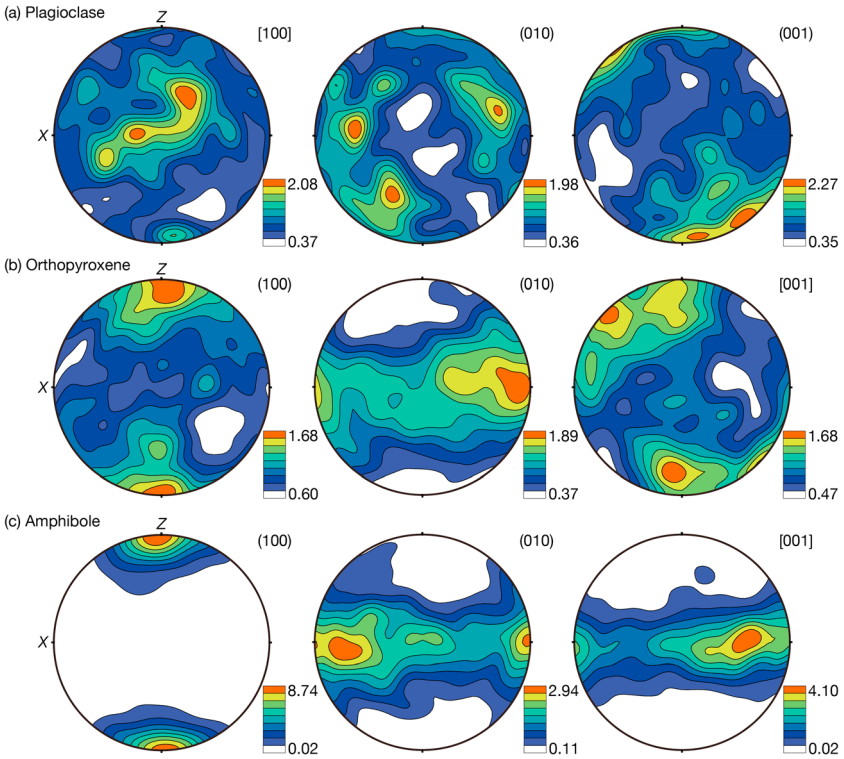

Figure 8. Crystallographic orientations of the recrystallized grains of plagioclase and orthopyroxene in the monophase plagioclase layer and amphibole grains in the layer of orthopyroxene-amphibole mixture. All the pole figures show grain fabrics (i.e., one point represent the crystallographic orientation of a grain). Equal-area, upper-hemisphere stereographic projections in the strain reference frame, with the foliation (*XY* plane) vertical and striking E-W, and lineation (*X* direction) horizontal, trending E-W. Contours refer to multiples of the uniform distribution. (a) (010) and (001) planes, and [100] axes of plagioclase grains. (b) Pole figures of poles to (100) and (010) planes, and [001] axes of orthopyroxene grains. (c) Pole figures of poles to (100) and (010) planes, and [001] axes of amphibole grains.

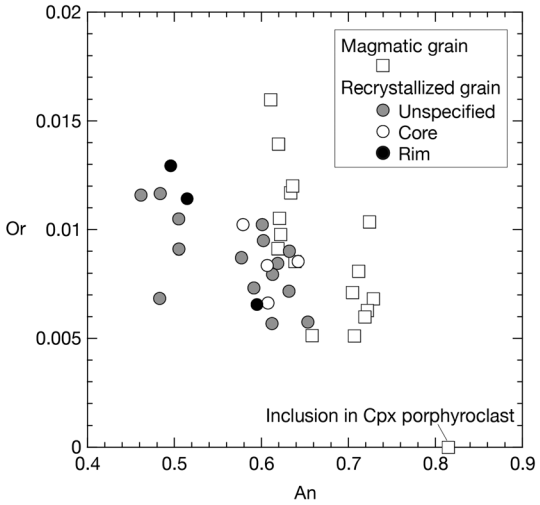

Figure 9. Plagioclase chemical compositions. The recrystallized grains have lower An contents than the magmatic porphyroclasts. For the recrystallized grains, An contents in the cores are higher than those in the rims. Extremely high-An inclusions are found in clinopyroxene porphyroclasts. Unspecified grains refer to analyses of grains where the distinction between core and rim part was not possible due to the small grain size.

The clinopyroxenes have X_{Mg} values of ~0.8–0.85 and Al contents less than 0.2 atoms per formula unit (a.p.f.u.) (Figure 10a). Fine-grained recrystallized grains usually have lower Al contents (<~0.05 a.p.f.u.) than the magmatic porphyroclasts, suggesting formation at lower temperatures [e.g., *Anovitz*, 1991]. The wollastonite mole fractions ($X_{Wo} = Ca/(Ca + Mg + Fe^{2+})$) of the recrystallized and magmatic clinopyroxenes are higher than 0.48. There is no systematic compositional zoning in neither the porphyroclasts nor the recrystallized grains, and no systematic chemical changes have been observed at the margins of the clinopyroxene porphyroclasts. The orthopyroxenes have X_{Mg} values of ~0.62–0.7 and Al contents that are less than 0.1 a.p.f.u. (Figure 10b). There is no systematic compositional zoning in neither the magmatic porphyroclasts nor the recrystallized grains, although the Al contents are lower in the recrystallized grains. The X_{Wo} values of the recrystallized and magmatic orthopyroxene are ~0.02. Orthopyroxene fragments within intragranular porphyroclast fracture zones

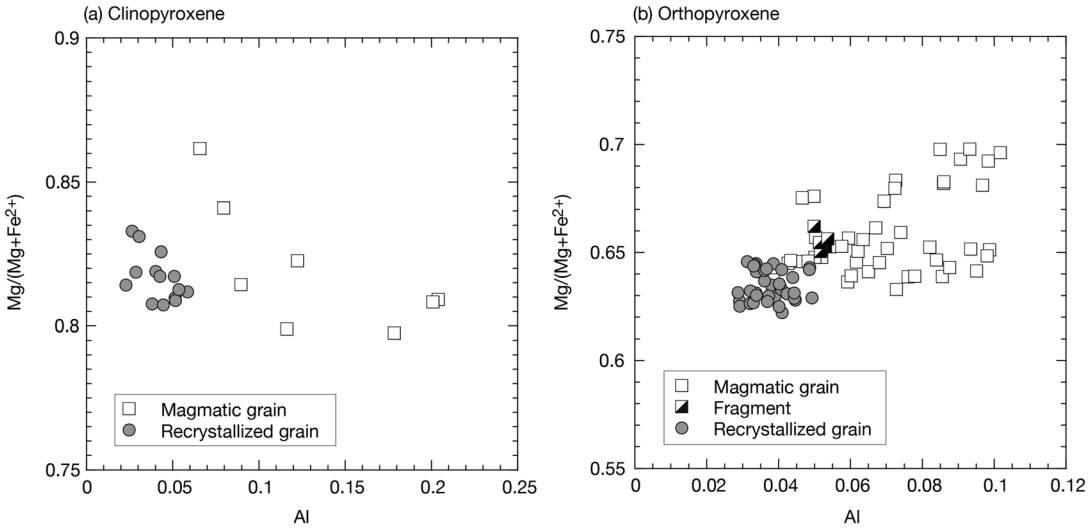

Figure 10. Pyroxene chemical compositions. (a) Clinopyroxene. (b) Orthopyroxene. The Al contents in the recrystallized grains are lower than in the magmatic grains. Fragments of the intragranular fracture zones within a magmatic porphyroclast have a compositional range between that of the recrystallized grains and the porphyroclasts.

have compositional ranges that lie between those of the recrystallized grains and the porphyroclasts (Figure 10b).

The amphiboles are calcic (hornblende) and have variable Si contents (Figure 11). The values of X_{Mg} (= Mg/(Mg + Fe^{2+})) range from 0.75 to 0.85. The amphiboles display a positive relationship between A-site occupancy and ^{iv}Al, suggesting edenite substitution; however, the slope is less than unity, implying some tschermakitic substitution of ^{iv}Al for Si. Compositional zoning in amphibole is common. Most cores of grains have higher X_{Mg} than rims (visible by darker cores than rims; Figure 4a). The higher X_{Mg} cores usually have lower Al contents (Figure 5c). Although there is some nonsystematic variation in core and rim compositions (Figure 11), the general trend described above is most common. There is a difference in the composition between the amphibole grains in different layers; the aluminum contents in amphibole grains in the vicinity of clinopyroxene are higher than those close to orthopyroxene (Figure 5c). These observations indicate that equilibrium of phase is achieved at a local scale (few to tens of microns).

5. Pressure-Temperature-H_2O Conditions

5.1. Pressure-Temperature Conditions

The fact that plagioclase and pyroxene grains show a systematic difference in composition between the recrystallized grains and the porphyroclasts indicates an adjustment of the composition to a new equilibrium composition during recrystallization. Furthermore, in fractures and shear zones in the Hasvik gabbro, the formation of metamorphic amphibole at the expense of magmatic pyroxene and plagioclase is observed. Thus, the syndeformational recrystallization can be described by the following reactions [*Beach*, 1980], taking clinopyroxene (cpx) and orthopyroxene (opx) separately:

$$9\ \text{cpx} + \text{plagioclase} + 12H^+ = 2\ \text{edenite(hornblende)} + 6Ca^{2+} + 9\ \text{quartz} + 4H_2O \quad (1a)$$

$$9\ \text{opx} + \text{plagioclase} + 3Ca^{2+} + 5H_2O = 2\ \text{edenite(hornblende)} + 6H^+ \quad (1b)$$

Quartz grains are commonly found in the shear zones together with amphibole, consistent with reaction (reaction (1a)). The newly formed amphibole grains are also found within intragranular shear zones crosscutting magmatic pyroxenes, suggesting a lesser involvement of plagioclase, indicating the following reactions [*Beach*, 1980]:

$$5\ \text{cpx} + 6H^+ = \text{tremolite–actinolite} + 3Ca^{2+} + 2\ \text{quartz} + 2H_2O \quad (2a)$$

$$5\ \text{opx} + 2Ca^{2+} + 3\ \text{quartz} + 3H_2O = \text{tremolite–actinolite} + 4H^+ \quad (2b)$$

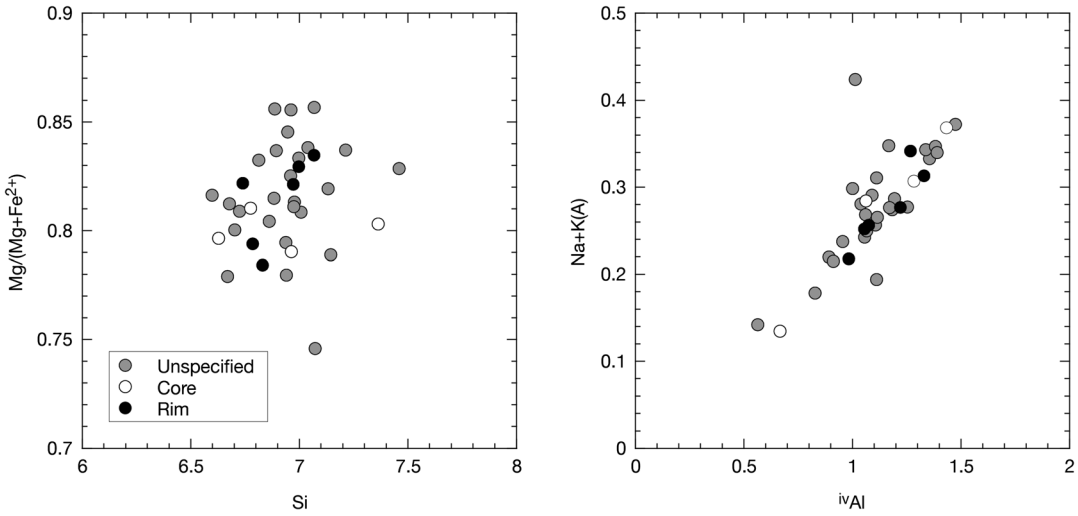

Figure 11. Amphibole chemical compositions. Although there is a difference in the composition between the amphibole cores and rims, systematic compositional variations between cores and rims cannot be observed. However, most cores of grains have higher X_{Mg} than rims (visible by darker cores than rims; Figure 4a).

However, the amphiboles found in these intragranular shear zones are not always more actinolitic than the amphiboles related to reactions (1a) and (1b). The magmatic pyroxenes have high Al contents (Figure 10) and may provide some of the Al in the amphiboles.

Fine-grained clinopyroxene and orthopyroxene grains coexist with amphibole, and their compositions differ from that of the larger magmatic crystals so that particularly the Al contents are lower in the fine-grained pyroxenes. The recrystallized plagioclase grains have lower anorthite contents than the nearby porphyroclasts. These observations suggest that the recrystallized pyroxene and plagioclase grains with the compositions different from the magmatic ones have crystallized by a retrograde (with respect to magmatic crystallization) metamorphic reaction, and they are inferred to be in local equilibrium with amphibole produced by hydration during this retrogression. The compositional variations may have resulted from $(NaAl)([\ ]Si)_{-1}$ and $(NaSi)(CaAl)_{-1}$ exchange between plagioclase and amphibole, as represented by the following reactions [*Holland and Blundy*, 1994]:

$$\text{edenite} + 4\ \text{quartz} = \text{tremolite} + \text{albite} \quad (3a)$$

$$\text{edenite} + \text{albite} = \text{richterite} + \text{anorthite} \quad (3b)$$

Based on the mineral chemistry of the recrystallized plagioclase and amphibole, some conventional thermobarometers such as the amphibole-plagioclase NaSi-CaAl exchange thermometer [*Holland and Blundy*, 1994] and the garnet-free, hornblende-plagioclase barometer formulated based on the reaction tremolite + tschermakite + 2 albite = 2 pargasite + 8 quartz [*Bhadra and Bhattacharya*, 2007] have been used to estimate pressure-temperature conditions at the time of fracturing and subsequent fluid infiltration. Care was taken to use compositions indicating local equilibrium because bulk equilibrium has not been observed in the ultramylonites. Temperatures are calculated for reaction (3b), useful for assemblages lacking quartz. Typical temperature and pressure uncertainties are ±40°C and ±200 MPa, respectively [*Holland and Blundy*, 1994; *Bhadra and Bhattacharya*, 2007]. The equilibrium was considered as local, on the scale of tens of microns, because amphibole compositions vary significantly even within a single thin section. We used the rim compositions of recrystallized minerals in adjacent pairs to estimate *P-T* conditions. Amphibole formulae were recalculated using the calculation schemes of *Holland and Blundy* [1994], *Dale et al.* [2000], and *Bhadra and Bhattacharya* [2007]. The results of our *P-T* estimates are listed in Table 2 and are shown in Figure 12. The temperatures range from ~700 to 750°C and pressures from ~0.5 to 0.6 GPa.

5.2. H_2O Content of the Assemblage

The formation of amphibole from plagioclase and pyroxene requires the infiltration of aqueous fluids. To evaluate the water content of mineral paragenesis, we have calculated equilibrium phase diagrams for the

Table 2. Results of *P-T* Estimates

	Amphibole[a]												
	T1-Site		M2-Site			M4-Site		A-Site			Plagioclase	*P-T* estimates		
	X_{Si}	X_{Al}	X_{Al}	X_{Fe2+}	X_{Fe3+}	X_{Na}	X_{Ca}	X_{Na}	X_{K}	$X_{[\ ]}$	X_{Ab}	P (GPa)	T_1 (°C)	T_2 (°C)
Pair#1	0.730	0.270	0.229	0.088	0.171	0.097	0.888	0.113	0.113	0.774	0.42	0.54	671	747
Pair#2	0.708	0.292	0.235	0.101	0.170	0.073	0.929	0.155	0.126	0.719	0.52	0.50	673	699
Pair#3	0.655	0.345	0.286	0.105	0.167	0.086	0.917	0.179	0.170	0.651	0.52	0.59	683	707
Pair#4	0.739	0.261	0.179	0.097	0.195	0.060	0.794	0.132	0.098	0.770	0.42	0.55	701	754

[a]Amphibole formula is estimated by the calculation scheme of *Holland and Blundy* [1994], *Dale et al.* [2000], and *Bhadra and Bhattacharya* [2007]. Pressure (*P*) in GPa; Temperature (*T*) in °C. *P* from *Bhadra and Bhattacharya* [2007] at temperature of 700°C; T_1 and T_2 based on *Holland and Blundy* [1994] for the reactions edenite + 4 quartz = tremolite + albite and edenite + albite = richterite + anorthite, respectively, at pressure of 500 MPa. Typical temperature and pressure uncertainties are ± 40°C and ± 200 MPa, respectively.

Hasvik gabbro. Pseudosections were calculated for the system Na_2O-CaO-FeO-MgO-Al_2O_3-SiO_2-H_2O by forward modeling using Perple_X 6.6.6 [*Connolly*, 2005] and the internally consistent thermodynamic data set of *Holland and Powell* [1998, upgraded 2002]. We used the solution models of *Newton et al.* [1980] for plagioclase; *Dale et al.* [2005] for amphibole, clinopyroxene, and orthopyroxene; *Holland and Powell* [1996] for garnet; and *Holland et al.* [1998] for chlorite. The effective bulk-rock composition used in the calculations was estimated by EDS analysis for specific areas (~0.6 mm^2 and ~0.3 mm^2) covering representative mineral assemblage of the shear zones: SiO_2 = 50.77, TiO_2 = 0.36, Al_2O_3 = 17.59, FeO = 6.75, MnO = 0.13, MgO = 8.02, CaO = 10.13, Na_2O = 2.50, and K_2O = 0.45 (in wt.%). This effective bulk-rock composition is similar to the averaged bulk-rock composition of rocks from the Basal Zone of the Hasvik Layered Intrusion [*Tegner et al.*, 1999]. In the calculation, the weight ratio of oxides is fixed. We assume that the fluid is of pure H_2O, although we do not know exactly the concentration of other components (i.e., NaCl and CO_2) in the fluid. As there are no carbonate minerals in shear zones, the effect of CO_2 concentration in the fluid on the mineral assemblage is assumed to be negligible.

The pseudosections of pressure versus temperature (*P-T*), of H_2O varying content versus temperature (*T-X*), and of H_2O versus modal abundances of the constituent minerals are shown in Figure 12. The *P-T* estimates using hornblende-plagioclase thermobarometry are also shown in the *P-T* pseudosections for the cases of H_2O = 0.1 and 0.2 wt.%. The estimated conditions of *P* and *T* from the thermobarometry plot in the stability fields of orthopyroxene + amphibole + plagioclase + clinopyroxene ± quartz for the cases of 0.1 and 0.2 wt.% H_2O (Figure 12a). The fine-grained clinopyroxene and orthopyroxene grains have compositions different from the magmatic porphyroclasts (Figure 10), suggesting their metamorphic origin. Quartz coexists with the other recrystallized minerals (Figures 5a and 5b). The mineral assemblages containing quartz is stable at the conditions of higher pressures or lower H_2O contents. To form a mineral paragenesis containing quartz, H_2O contents have to be lower than ~0.15–0.2 wt.% at the time of the hydration reaction and the deformation of the shear zones (Figure 12b). Furthermore, for H_2O contents lower than ~0.5 wt.%, H_2O contents are not saturated in the shear zone below the temperature conditions of ~780°C. In temperature-water activity (a_{H2O}) space, under the pressure condition of 500 MPa, the boundary between the stability fields of orthopyroxene + amphibole + plagioclase + clinopyroxene ± quartz is located at a_{H2O} of ~0.7 for 750°C. This means that a pure H_2O fluid (a_{H2O} = 1) infiltrates the rock but is then absorbed so that the rock equilibrates under the fluid-deficient conditions (so that $a_{H2O} < 1$). The changes of modal abundance of the constituent minerals are shown in Figure 12c. With increasing H_2O contents, modal amounts of plagioclase, pyroxenes, and quartz decrease linearly, but those of amphibole increase; quartz and clinopyroxene would disappear above H_2O contents of ~0.15 wt.% and of ~0.55 wt.%, respectively. Thus, the observed mineral assemblage is only stable at H_2O-undersaturated conditions of ~0.15 to 0.2 wt.% H_2O.

5.3. Porosity

In Figure 13a, pores (yellow) are segmented by binary thresholding and their surfaces rendered. Orthopyroxene (blue/white), amphibole or clinopyroxene (red), and plagioclase (black) are shown as rendered volumes. The cracked regions of the gabbro show crack fillings of typically plagioclase/pyroxene or plagioclase/amphibole composition (Figures 3 and 13a). Amphibole is also forming at the rims of

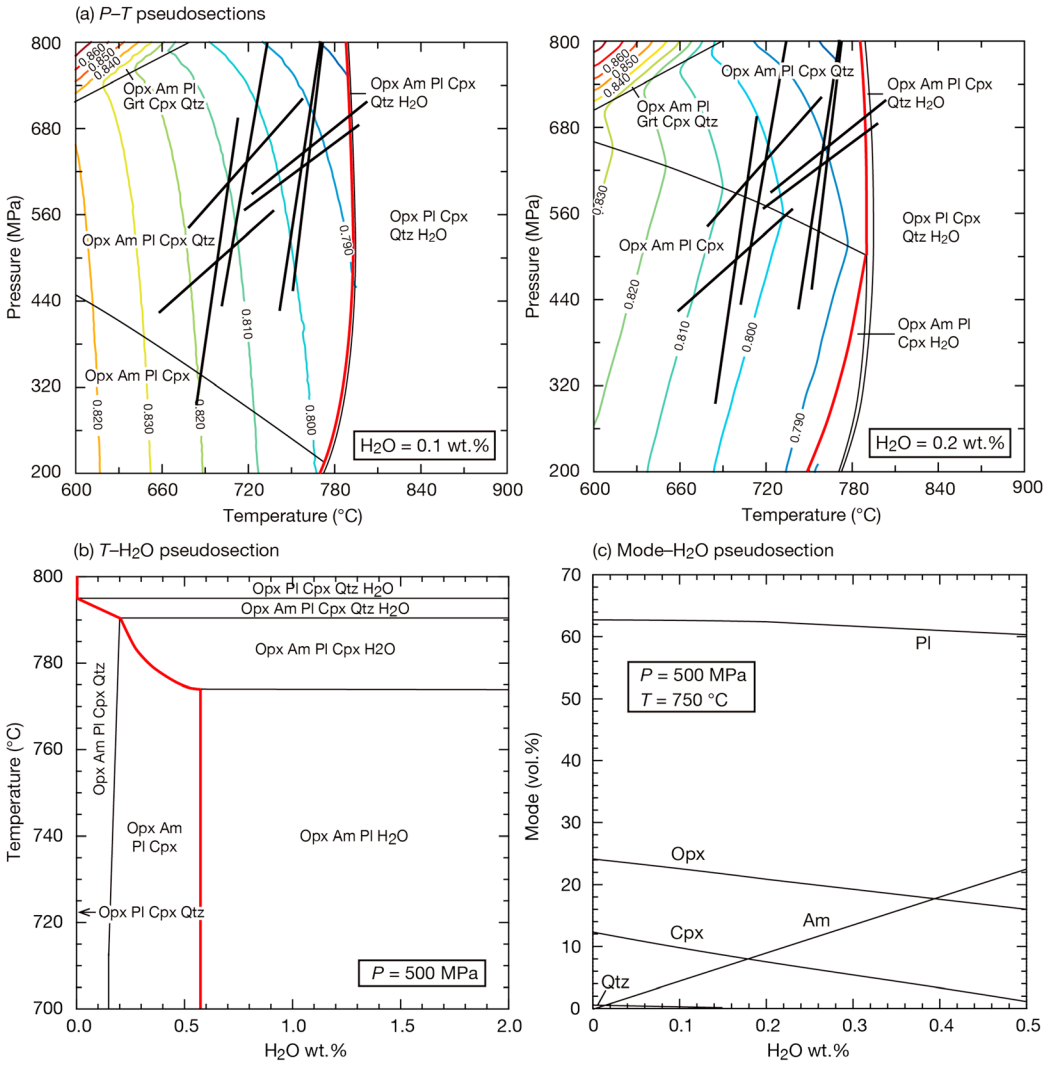

Figure 12. Pseudosections in the system Na_2O-CaO-FeO-MgO-Al_2O_3-SiO_2-H_2O calculated for the compositions of which the weight ratio of oxides is fixed as SiO_2:Al_2O3:FeO:MgO:CaO:Na_2O = 50.77:17.59:6.75:8.02:10.13:2.50. The thick red line is the H_2O saturation line. (a) *P-T* pseudosections. Results for the cases of H_2O = 0.1 and 0.2 wt.% are shown. Contours represent the values of X_{Mg} of amphibole. The thick lines represent results of conventional thermobarometric calculations. The steeply and gently inclining thick lines represent results of amphibole-plagioclase thermometer of *Holland and Blundy* [1994] and barometer of *Bhadra and Bhattacharya* [2007], respectively. (b) Pseudosection of H_2O versus temperature (P = 500 MPa). (c) Pseudosection of H_2O versus modal abundances (P = 500 MPa, T = 750°C). See text for details.

orthopyroxene as overgrowths. It is remarkable that there is no porosity associated with the transgranular cracks across several grains (Figure 13a). Most likely, the absence of porosity is due to the fact that amphibole has a lower density than pyroxene, so that the amphibole growth during the crack-filling is accompanied with a positive volume change, which seals the pore space effectively. Pure plagioclase domains show extensive isolated porosity away from cracks (Figure 13a). Porosity in feldspar grains is common due to the ordering and exsolution processes during temperature changes [e.g., *Walker et al.*, 1995; *Parsons et al.*, 2010].

During viscous mylonite deformation, the porosity is heterogeneously distributed in the mixed phase and monomineralic layers (Figures 13b and 13c). The monomineralic plagioclase layers show significantly lower porosity than the mixed phase layers (pyroxene/amphibole and plagioclase/pyroxene; Figures 13b and 13c). In particular, the plagioclase/amphibole layers show a high porosity. The pores have a small size of several microns and are situated at the grain boundaries of the small grains of the ultramylonite.

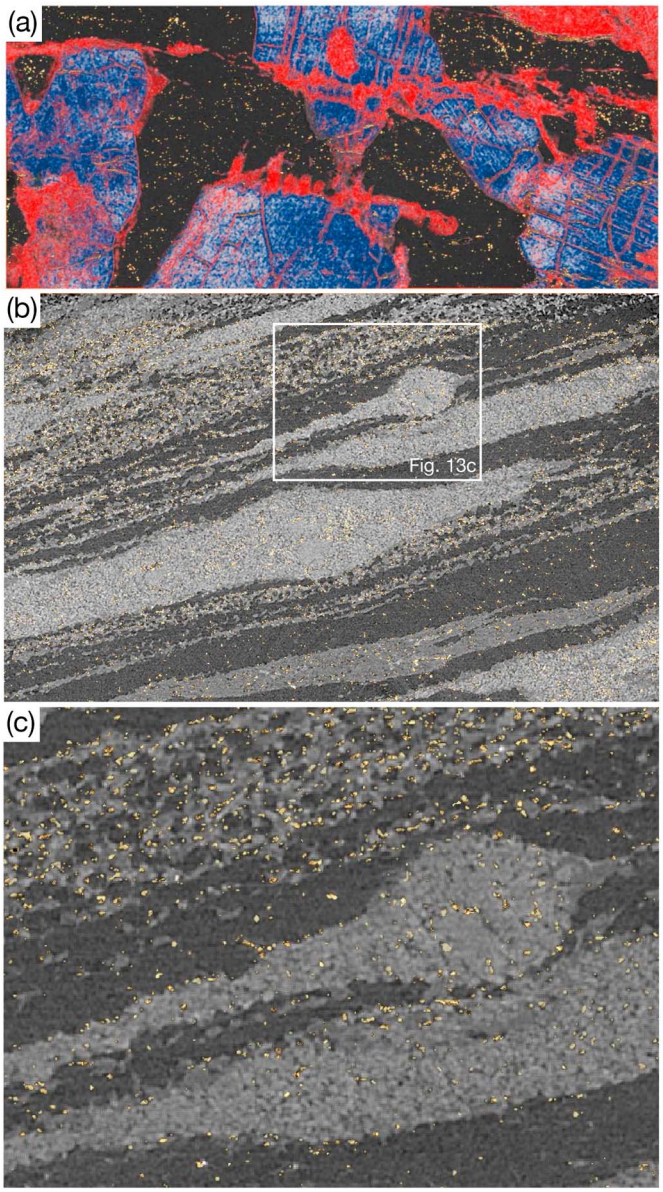

Figure 13. X-ray microtomographic images. (a) Region of cracked gabbro. Blue/white: orthopyroxene; red: amphibole or clinopyroxene; black: plagioclase; and yellow: porosity. The cracks filled with amphibole do not show any porosity. Porosity is only present inside plagioclase grains. There is a clinopyroxene grain in the upper right corner of the image and a clinopyroxene inclusion within the orthopyroxene grain in the upper half and middle of the image. Sample SIP II-5b-3, width of view is 2.569 mm. (b) Layered ultramylonite. Dark gray: plagioclase; medium gray: amphibole; light gray: orthopyroxene; and yellow: porosity. The monomineralic layers (here plagioclase) consistently show a lower porosity than the mixed phase layers. Sample SIP II-2A, width of view is 2.516 mm. (c) Close-up view of the area surrounded by the white frame in Figure 13b.

6. Discussion

The studied deformation zones show a transition from fracturing to subsequent viscous deformation. The *P-T* conditions of the deformation are of intermediate *P* granulite facies conditions (700–750°C, 0.5–0.6 GPa), comparable with those determined by *Tegner et al.* [1999] for the contact aureole and by *Elvevold et al.* [1994] of the formation of a mylonitic foliation in the Seiland Igneous Province metagabbros from the Øksfjord area. Thus, the deformation occurs on a small scale but is widespread over a larger region. In the following, the *P-T-*X_{H2O} conditions of the deformation, the deformation mechanisms, and their transitions will be discussed.

6.1. *P-T-*X_{H2O} Conditions of Deformation

The microstructural observations described above suggest that the recrystallized pyroxene and plagioclase grains with the compositions different from the magmatic porphyroclasts have crystallized by a retrograde metamorphic reaction. The compositional differences between the porphyroclasts and the recrystallized grains cannot be attributed to diffusional modification during high-*T* metamorphism. The rates of Al diffusion in clinopyroxene and the NaSi-CaAl exchange in plagioclase are so slow that growth zoning is commonly preserved even at granulite-facies metamorphism. The extrapolated diffusion coefficient *D* [*Cherniak and Liang*, 2012] is based on the experimental data for Al diffusion in diopside [*Sautter et al.*, 1988] which is approximately $10^{-25-24}\,m^2\,s^{-1}$ at 750°C. For a duration of 1 Myr, the diffusion coefficient yields a characteristic length ($=\sqrt{(Dt)}$) of ~2–6 μm, suggesting that at 750°C modification of clinopyroxene composition with the grain size of ~4–12 μm can be completed over a period of 1 Myr. However, the true activation energy for Al diffusion in clinopyroxene is not known, and there is a long extrapolation to lower temperature; hence, the diffusion coefficient for Al has large uncertainty (several orders of magnitude). The diffusion coefficient for coupled CaAl-NaSi diffusion in dry plagioclase is on the order of $10^{-28}\,m^2\,s^{-1}$ at 750°C [*Grove et al.*, 1984], and the characteristic length scales are shorter than those for Al diffusion in diopside. Compositional modification of the small

plagioclase clasts after fracturing is unlikely to occur at temperatures of 700–750°C, but the Al contents of the fine-grained pyroxene clasts could be modified. In such a case, the dissolved Al in pyroxene will segregate on or near its grain boundary [*Skemer and Karato*, 2007], and the Al contents in the pyroxenes decrease before hydration, whereas plagioclase compositions will not be changed. Furthermore, if fracturing had occurred at temperatures greater than 750°C, the compositions of very fine grained pyroxene clasts could have been changed significantly. However, the margins of the pyroxene porphyroclasts do not display any systematic chemical variations, suggesting that diffusional modification was not effective. This condition may imply that duration of the high-temperature conditions would be shorter than 1 Myr.

The aluminum contents in amphibole grains in the vicinity of clinopyroxene are higher than those close to orthopyroxene (Figure 5c), indicating local equilibrium. The recrystallized clinopyroxene and orthopyroxene develop around the pyroxene porphyroclasts (Figure 5a); it implies that local equilibrium controls the abundance and distribution of new phases. Few newly formed clinopyroxene grains occur in the matrix of the orthopyroxene-dominated area, and vice versa, suggesting that nucleation and growth of new grains were controlled by the local effective bulk-rock composition. These observations suggest that chemical equilibrium was achieved only locally (i.e., over a few or tens of microns), consistent with the fluid-deficient conditions inferred from pseudosection modeling (Figure 12).

During the hydration reactions and formation of the ultramylonites in the Hasvik gabbro, the amount of H_2O is determined to be ~0.15–0.2 wt.% from pseudosection analysis of the syndeformational mineral assemblage. The different chemical compositions of recrystallized amphiboles on the thin section scale (Figure 5c) may be caused by (1) a local difference in the effective bulk-rock composition, (2) changing *P-T* conditions, and (3) changing H_2O contents. The zonation trend of amphibole (higher X_{Mg} in cores of grains) may indicate a retrograde evolution toward lower temperatures and pressures during amphibole growth (changing *P-T* conditions). This is a likely possibility. The amphibole zonation may also indicate higher H_2O contents. For example, the pseudosection analysis shows that X_{Mg} values of amphibole change from 0.803 to 0.794, with changing H_2O contents from 0.1 to 0.2 wt.% (Figure 12a), at the conditions of 750°C and 500 MPa. The compositional zonation trend in individual amphibole grains is characterized by higher X_{Mg} values in the core than in the rim (Figures 4a, 5a, and 5b), consistent with lower H_2O contents in shear zones during the initial growth of amphibole cores. Thus, the zonation trend of amphibole may indicate increasing H_2O contents during ultramylonite deformation over time.

6.2. Deformation Mechanisms and Shear Zone Formation

6.2.1. Fracturing

The initial fracturing of the gabbro at fairly high confining pressures and at high temperatures is a rather unusual occurrence, unless high pore pressures are involved. For the seismogenic zone of the upper ~12 km of the crust, hydrostatic pore pressure conditions are assumed [e.g., *Zoback and Townend*, 2001], but the depth, where the gabbro deformation occurred, is ~20 km. At these depths, pore space is expected to be isolated and/or permeability very limited [e.g., *Wark and Watson*, 1998], and thus, local pore pressures greater than hydrostatic (approaching lithostatic) may be assumed. Under such conditions, the mechanical behavior of the rock is probably more dependent on the volume fraction of pore space (a value which is expected to be very small) rather than the pore pressure itself (which is assumed to be close to lithostatic). If the volume fraction increases, there will be a threshold, where rock becomes mechanically unstable and will fail.

Unfortunately, there are few quantitative experimental data for the mechanical effects of small fractions of pore fluid under lithostatic pressure (=undrained experiments; this does not consider effects of H_2O contents on the order of a few hundred or thousand $H/10^6$ Si required to induce H_2O weakening in silicates = "wet" samples). However, *Kronenberg and Tullis* [1984] have investigated the strength of quartzite at different H_2O contents, trying to determine the threshold values, where rock becomes mechanically unstable at elevated volume fractions of H_2O. They have not found systematic strength differences for H_2O contents up to 0.5 wt.%. *Stünitz and Tullis* [2001] have tested plagioclase at different H_2O contents, and there is no systematic difference in strength up to 0.3 wt.% H_2O. *Negrini et al.* [2014] have observed systematically weaker behavior of feldspar above 0.2 to 0.3 wt.% H_2O. From this limited database, it appears that at the low H_2O contents of 0.15 to 0.2 wt.% determined for the Hasvik gabbro (Figure 12), it is

unlikely that for such small volume fractions even lithostatic pore pressures have had a strong mechanical effect on the rock strength.

The circumstantial evidence given above implies that the initial fracturing in the Hasvik gabbro at high temperatures and intermediate confining pressures has occurred at high differential stresses in the absence of significant pore pressure effects. This result concurs with other examples of inferred high strength for the lower crust [e.g., *Maggi et al.*, 2000; *Jackson*, 2002]. High differential stresses (at least on the order of the confining pressure) indicate that the fracturing could have occurred seismically.

The recrystallized plagioclase has a different composition from the host plagioclase, in the fractures, as well as in the ultramylonites (Figures 4b and 9). These observations suggest that the plagioclase in fractures developed at first from brittle fracturing of the host grains but that this process was followed by nucleation and/or growth after the fracturing.

The fact that fracture zones contain grains with a narrow grain size range, which is similar to that of the ultramylonites, indicates that the present size distribution is not the result of a cataclastic process alone, because that would result in a large range of sizes [e.g., *Sammis et al.*, 1986; *Keulen et al.*, 2007]. Cataclastic fracture zones have been observed in experimental studies on feldspar and quartz (e.g., *Stünitz et al.* [2003] for plagioclase and *Vernooij et al.* [2006] and *Trepmann et al.* [2007] for quartz). In these experiments, no crystallographic relationship between the orientations of the recrystallized and host grains was observed. The fact that the small grains in these experiments displayed rounded shapes rather than clast-like irregular outlines suggested that their grain boundaries had been mobile and that their present configuration was the result of grain boundary migration [*Stünitz et al.*, 2003] or static grain growth [*Trepmann et al.*, 2007]. In fracture zones, nucleation of new grains may have occurred on small fragments. In any case, the different composition of small grains and their size distribution indicates that the present grains are the result of nucleation and growth.

6.2.2. Viscous Deformation

Subsequent to fracturing, the rock has deformed by viscous deformation process producing the ultramylonites. Within the ultramylonites of the Hasvik gabbro, plagioclase and pyroxene adjust their composition to the ambient P-T-X_{H2O} conditions of deformation, while the original magmatic grains have maintained their composition outside the ultramylonites and fracture zones. Most likely, this is because additional driving potential for the reactions has been provided by strain energy [*Stünitz*, 1998; *Wintsch and Yi*, 2002], and infiltration of H_2O necessary for amphibole formation has occurred in the deformation zones.

The small observed grain size in the phase mixtures (3 to 20 μm), the well dispersed mixing of phases, and the crystal size distributions indicate that deformation has taken place by grain boundary sliding and diffusive mass transfer processes (diffusion creep) in the ultramylonites. EBSD analysis shows that plagioclase grains virtually lack a preferred crystallographic orientation, and the weak orthopyroxene CPO is not consistent with dislocation creep by common slip systems (Figure 8). The lack of a plagioclase and the weak orthopyroxene CPO support the inference that the fine-grained plagioclase and orthopyroxene in the shear zones deformed mainly by grain-size-sensitive creep (grain boundary sliding and/or diffusion creep) during and/or after the nucleation and growth of secondary plagioclase and orthopyroxene. The amphibole grains have a strong CPO, but these observations (fine grain size of all phases, no CPO in plagioclase, and strong CPO type in amphibole) are exactly the same as those from experiments on amphibolite described by *Getsinger and Hirth* [2014], where they conclude, based on stress exponents, that the deformation has taken place by diffusion creep. The amphibole CPO most likely results from oriented growth and/or rigid body rotation during deformation, as concluded for other natural examples by *Berger and Stünitz* [1996], *Imon et al.* [2004], and *Getsinger et al.* [2013]. Thus, the dominant deformation mechanism in the ultramylonites is concluded to be grain boundary sliding accommodated by diffusive mas transfer, with solution-precipitation processes.

Crystal size distributions (CSDs) for minerals in the ultramylonite have a longer tail for grain sizes less than the mean, whereas the cutoff is quite sharp above d_{mean} (Figure 6). These CSDs are comparable with the lognormal or Lifshitz-Slyosov-Wagner (LSW) distributions [e.g., *Cashman and Ferry*, 1988; *Miyazaki*, 1991; *Yoshino and Yamazaki*, 2007]. The LSW distribution is characterized by the shape of a crystal size distribution with a peak skewed toward larger grain sizes, a tail extending to the smaller grain sizes, and

a sharp cutoff at grain size ~1.5–2 times the average size. LSW distributions for metamorphic rocks result from the initial continuous nucleation and growth of crystals followed by subsequent growth of larger grains at the expense of smaller crystals, which are undergoing dissolution (Ostwald ripening) [e.g., *Cashman and Ferry*, 1988; *Joesten*, 1991]. The crystal size distributions obtained by grain growth in fluid- or melt-bearing systems tend to change from the LSW distribution toward a lognormal distribution [*Yoshino et al.*, 2006]. As the observed distributions in the ultramylonites are intermediate between these cases, it is inferred that the CSDs of the recrystallized minerals have been modified by dissolution-precipitation processes. In the presence of aqueous fluids, the dissolution of grains or parts of grains with high normal stresses or with high internal energy is more easily activated than dislocation creep, and dissolution and precipitation creep are the dominant deformation mechanism of diffusion creep [*Wintsch and Yi*, 2002].

6.3. Evolution of Porosity During Deformation

During initial fracturing of the gabbro, aqueous fluid infiltration occurs through the crack system. This process is evident from amphibole formation and the localized change in plagioclase composition in the cracks. Although the permeability has to be increased for this process, the porosity during the recrystallization within cracks decreases, as there is no detectable porosity on the order of (i.e., $>2\,\mu m$) in these cracks today (Figure 13a).

The displacement along these cracks is very small (Figure 3), so that the main processes after crack formation are fluid infiltration and recrystallization of the crack fills. This represents the porosity development in a rather static system, i.e., the dilatant system is not moving but only filled by minerals, which partly have a larger volume (amphibole).

The porosity development in a dynamic system is quite different. In the ultramylonites, porosity is present in most of the layers (Figure 13b), and the total porosity in the shear zone is higher than in the host rock. The fluid content in our ultramylonites has been estimated to ~0.15 to 0.2 wt.%. Similar values from deformation experiments, usually with ~0.1 wt.% H_2O, are commonly referred to as wet [e.g., *Rybacki and Dresen*, 2004]. Those conditions in experiments are sufficient for hydration reactions and diffusion-accommodated grain boundary sliding to take place [*Stünitz and Tullis*, 2001]. If connected porosity is dynamically created by grain boundary sliding, the amounts of H_2O at grain boundaries may continue to stay constant or even increase during deformation. The slight increase of H_2O content during viscous deformation may indicate additional connected porosity during creep. Fluid-filled pores can communicate through grain boundaries during deformation; permeable porosity is dynamically created by viscous grain boundary sliding, which can produce creep cavitation, dissolution, and precipitation [*Rybacki et al.*, 2008; *Fusseis et al.*, 2009].

The deformation mechanism in ultramylonites is inferred to be diffusion creep, involving a combination of grain boundary sliding and dissolution-precipitation, suggesting that connected porosity was created during the deformation. In the shear zones, there is a difference in the pore density between individual layers. The pore density in the mixed layers is higher than that in the monophase plagioclase layers, suggesting a heterogeneous development of porosity in different parts of the rock. The reason could be that the grain-boundary properties in the mixed layers are different from those of the monomineralic layers, i.e., that phase boundaries may develop creep cavitation more easily than grain boundaries.

6.4. Rheological Implications

Our results indicate that the Hasvik gabbro was subjected to very high stress levels at the time of brittle fracturing. The brittle to viscous transition occurs at the temperature, where dislocation creep mechanisms can be activated to accommodate strain rates required for deformation [e.g., *Kohlstedt et al.*, 1995]; plasticity can be activated in plagioclase at ~450°C [e.g., *Rybacki and Dresen*, 2004], while plasticity in clinopyroxene is not predicted below 500°C [e.g., *Mauler et al.*, 2000]. The temperatures under which the fracturing and subsequent fluid infiltration occurred are estimated to have been 700–750°C, and at such temperatures, crystal plastic deformation is expected for plagioclase and pyroxene. On the other hand, cataclastic flow, associated with the brittle-ductile transition [e.g., *Tullis and Yund*, 1987], may occur at higher than expected temperatures if the stress levels are very high [*Hadizadeh and Tullis*, 1992], and this may be the case, for example, if coseismic loading is taking place [*Trepmann and Stöckhert*, 2003].

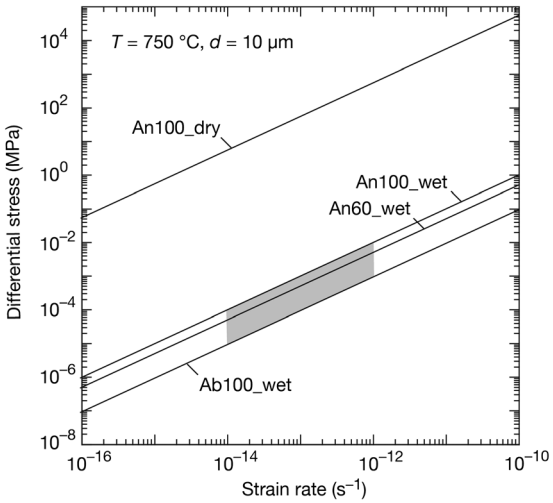

Figure 14. Stress versus strain rate for a plagioclase aggregate deformed by grain-size-sensitive creep at a temperature of 750°C and with a grain size of 10 μm. The constitutive equations of grain-size-sensitive creep (diffusion creep) for a dry anorthite aggregate (An100_dry; *Rybacki and Dresen* [2000]), a wet anorthite aggregate (An100_wet; *Rybacki and Dresen* [2000]), a wet labradorite aggregate (An60_wet; *Dimanov et al.*, unpublished; flow law creep parameters are listed in Table 1 of *Rybacki and Dresen* [2004]), and a wet albite aggregate (Ab100_wet; *Offerhaus et al.* [2001]) are used. The gray-shaded area shows the possible range of differential stress during the viscous deformation of the Hasvik gabbro.

Major earthquakes, which nucleate in the seismogenic zone, can cause faults to propagate well into the underlying ductile region at the stage of coseismic displacement [e.g., *Ellis and Stöckhert*, 2004]. This is predicted to create short-term high differential stresses, high strain rates, and related changes of pore fluid pressures in the ductile region near the tip of a seismically active fault in the lower crust. The rocks undergoing thermally activated viscous creep at low strain rates are expected to respond by both brittle and plastic deformation at high strain rates [e.g., *Trepmann et al.*, 2007]. The stage of quasi-instantaneous high-stress deformation during an earthquake is followed by creep during the decay of strain rates and postseismic stress relaxation [*Scholz*, 1989].

These processes may be recorded as microstructures characterized by initial brittle fracturing followed by viscous deformation, and the resulting microstructures would differ from those formed during a steady state deformation. In the Hasvik gabbro, we can recognize the initial fracturing and the subsequent grain-size-sensitive creep, and this suggests that they experienced very high stress levels at high temperatures with subsequent creep during lower stresses. Moreover, the incomplete metamorphic transformation of the Hasvik gabbro into amphibolite indicates limited infiltration of aqueous fluids, which may be facilitated by creep cavitation processes during viscous shearing.

For geologically realistic strain rates of ~$10^{-12}\,s^{-1}$ and temperatures determined for the deformation of ultramylonites (750°C), the constitutive equations for diffusion creep in plagioclase aggregates can be used to estimate the stress level applied to aggregates with the observed grain size of ~10 μm. The application of constitutive equations of grain-size-sensitive creep (diffusion creep) for a wet anorthite (An_{100}, 0.07 wt.% H_2O) aggregate [*Rybacki and Dresen*, 2000] and a wet labradorite (An_{60}, 0.3 wt.% H_2O) aggregate (*Dimanov et al.*, unpublished; flow law creep parameters are listed in Table 1 of *Rybacki and Dresen* [2004]) yield a shear stress of ~0.01 MPa (Figure 14). Most of the water in shear zones is structurally bound in amphibole; the flow law uses volume diffusion coefficients, and in the natural case, grain boundary diffusion is to be assumed. Thus, the wet flow laws [*Rybacki and Dresen*, 2000], determined for water conditions comparable to our estimated water contents, predict only a minimum value of the flow stress at a given strain rate. The estimated stress is comparable with the creep stress (<0.1 MPa) for a long-term viscous deformation during a seismic cycle using geodetic strain measurements and the viscosity estimates proposed by *Rybacki and Dresen* [2004]. It is also comparable with the stress estimated during low-frequency earthquakes at the base of the crust along the San Andreas Fault, where the earthquakes are triggered by a tidally induced shear stress of 1.77×10^{-4} MPa (differential stress of ~3.5×10^{-4} MPa) [*Thomas et al.*, 2009; *Getsinger et al.*, 2013]. Such low shear stresses suggest that the microstructures in the Hasvik gabbro shear zones formed during a large local stress drop related to postseismic stress relaxation.

The resulting microstructures of the shear zone are mylonitic, and although there are no strain markers, a shear strain of $\gamma = 10$ can be assumed as a conservative estimate. At the inferred strain rates of $10^{-12}\,s^{-1}$, it would take ~0.3 Myr to attain this strain. This time period appears to be too long for a seismic cycle, and thus, the viscous strain rates may have been even orders of magnitude higher than our estimate. Alternatively, at higher strain rates, the stresses could easily have been higher and still produce viscous deformation. In any case, it is important to point out that the potentially high strain rates during the

viscous deformation are the result of a transformation of the material properties after an initial brittle (high stress) deformation. It is the material transformation through chemical disequilibrium and nucleation of new phases which has caused the viscous deformation.

7. Conclusions

Localized deformation zones are developed in the Hasvik gabbro in the Seiland Igneous Province, northern Norway, and their development can be reconstructed as follows:

1. The initial mechanism of grain size reduction of the magmatic plagioclase and pyroxene is fracturing and subsequent nucleation and growth of new phases during hydration reactions. This process results in different compositions of recrystallized plagioclase, clinopyroxene, and orthopyroxene.
2. Based on conventional thermobarometric analyses, the shear zones of secondary plagioclase and amphibole have formed under conditions of ~700–750°C and ~0.5–0.6 GPa.
3. Based on the mineral paragenesis combined with the *P-T* estimates, H_2O contents in the shear zones have been less than 0.2 wt.% at the time of reaction and deformation.
4. The microstructures and the *P-T* conditions indicate high-temperature fracturing and the subsequent infiltration of aqueous fluids into the shear zones.
5. The crystallographic preferred orientations of plagioclase are random and those of orthopyroxene weak, both consistent with deformation of grain boundary sliding and diffusive mass transfer in the fine-grained aggregates after their nucleation and growth. Amphibole grains have strong CPOs, but these probably result from oriented growth and rigid body rotations during deformation, suggesting solution-precipitation creep as the dominant mechanism.
6. Dynamic porosity has been maintained during grain boundary sliding in ultramylonites, while hydration reactions in a static situation in cracks (producing less dense mineral assemblages) have lead to a sealing of the pore space.
7. The Hasvik gabbro experienced high stress levels at high temperatures (on the order of the confining pressure or even higher). The subsequent creep in ultramylonites took place during after a substantial stress drop to very low values of ~0.01 MPa. The stress drop is caused by a transformation of material properties (by nucleation of new phases), leading to viscous deformation after initial fracturing.

Acknowledgments

Erling J. Krogh Ravna is thanked for his guidance to the outcrops and useful information about the Hasvik gabbro. Christian Tegner provided us with the results of bulk-rock chemical analyses of the Hasvik gabbro. Atsushi Okamoto is thanked for his advice on thermodynamic calculations. Discussions with Pritam Nasipuri and Luca Menegon have improved some ideas of this work. This paper benefited from detailed and very constructive reviews by Erik Rybacki and Greg Hirth. Michael Walter is thanked for his editorial handling of the manuscript. This study was supported by the Research Council of Norway FRINAT program (191526) and the University of Tromsø to H. S., and by the OCU Overseas Research Fellowship and MEXT KAKENHI grant 26109004 to T.O. P.J. acknowledges support from the Czech Science Foundation research grant 14-15632S. The use of the Advanced Photon Source at Argonne National Laboratory was supported by the U.S. Department of Energy, Office of Science, Office of Basic Energy Sciences, under contract DE-AC02-06CH11357. T.O. will make numerical data used in generating the figures in this study available upon request.

References

Anovitz, L. M. (1991), Al zoning in pyroxene and plagioclase: Window on late prograde to early retrograde *P-T* paths in granulite terranes, *Am. Mineral.*, *76*, 1328–1343.

Beach, A. (1980), Retrogressive metamorphic processes in shear zones with special reference to the Lewisian complex, *J. Struct. Geol.*, *2*, 257–263, doi:10.1016/0191-8141(80)90058-9.

Berger, A., and H. Stünitz (1996), Deformation mechanisms and reaction of hornblende: Examples from the Bergell tonalite (Central Alps), *Tectonophysics*, *257*, 149–174, doi:10.1016/0040-1951(95)00125-5.

Bhadra, S., and A. Bhattacharya (2007), The barometer tremolite + tschermakite + 2 albite = 2 pargasite + 8 quartz: Constraints from experimental data at unit silica activity, with application to garnet-free natural assemblages, *Am. Mineral.*, *92*, 491–502, doi:10.2138/am.2007.2067.

Brander, L., H. Svahnberg, and S. Piazolo (2012), Brittle-plastic deformation in initially dry rocks at fluid-present conditions: Transient behaviour of feldspar at midcrustal levels, *Contrib. Mineral. Petrol.*, *163*, 403–425, doi:10.1007/s00410-011-0677-5.

Brodie, K. H., and E. H. Rutter (1985), On the relationship between deformation and metamorphism, with special reference to the behavior of basic rocks, in *Metamorphic Reactions*, edited by A. B. Thompson et al., Springer, New York.

Carter, N. L., A. K. Kronenberg, J. V. Ross, and D. V. Wiltschko (1990), Control of fluids on deformation of rocks, in *Deformation Mechanisms, Rheology and Tectonics*, edited by R. J. Knipe and E. H. Rutter, *Geol. Soc. London Spec. Publ.*, *54*, 1–13.

Cashman, K. V., and J. M. Ferry (1988), Crystal size distribution (CSD) in rocks and the kinetics and dynamics of crystallization. III. Metamorphic crystallization, *Contrib. Mineral. Petrol.*, *99*, 401–415, doi:10.1007/BF00371933.

Cherniak, D. J., and Y. Liang (2012), Ti diffusion in natural pyroxene, *Geochim. Cosmochim. Acta*, *98*, 31–47, doi:10.1016/j.gca.2012.09.021.

Connolly, J. A. D. (2005), Computation of phase equilibria by linear programming: A tool for geodynamic modeling and its application to subduction zone decarbonation, *Earth Planet. Sci. Lett.*, *236*, 524–541, doi:10.1016/j.epsl.2005.04.033.

Dale, J., T. Holland, and R. Powell (2000), Hornblende-garnet-plagioclase thermobarometry: A natural assemblage calibration of the thermodynamics of hornblende, *Contrib. Mineral. Petrol.*, *140*, 353–362, doi:10.1007/s004100000187.

Dale, J., R. Powell, R. W. White, F. L. Elmer, and T. J. B. Holland (2005), A thermodynamic model for Ca-Na clinoamphiboles in Na_2O-CaO-FeO-MgO-Al_2O_3-SiO_2-H_2O-O for petrological calculations, *J. Metamorph. Geol.*, *23*, 771–791, doi:10.1111/j.1525-1314.2005.00609.x.

Dallmeyer, R. D., J. G. Mitchell, T. C. Pharaoh, A. Reuter, and A. Andersen (1988), K–Ar and 40Ar/39Ar whole-rock ages of slate/phyllite from allochthonous basement and cover in the tectonic window of Finnmark, Norway: Evaluating the extent and timing of Caledonian tectonothermal activity, *Geol. Soc. Am. Bull.*, *100*, 1439–1501, doi:10.1130/0016-7606(1988)100<1493:KAAAAW>2.3.CO;2.

Daly, J. S., S. J. Aitcheson, R. A. Cliff, R. A. Gayer, and H. N. Rice (1991), Geochronological evidence from discordant plutons for a Late Proterozoic orogen in the Caledonides of Finnmark, northern Norway, *J. Geol. Soc. Lond.*, *148*, 29–40, doi:10.1144/gsjgs.148.1.0029.

De Bresser, J. H. P., J. H. Ter Heege, and C. J. Spiers (2001), Grain size reduction by dynamic recrystallization: Can it result in major rheological weakening, *Int. J. Earth Sci.*, *90*, 28–45, doi:10.1007/s005310000149.

Díaz Aspiroz, M., G. E. Lloyd, and C. Fernández (2007), Development of lattice preferred orientation in clinoamphiboles deformed under low-pressure metamorphic conditions. A SEM/EBSD study of metabasites from the Aracena metamorphic belt (SW Spain), *J. Struct. Geol.*, *29*, 629–645, doi:10.1016/j.jsg.2006.10.010.

Ellis, S., and B. Stöckhert (2004), Elevated stresses and creep rates beneath the brittle-ductile transition caused by seismic faulting in the upper crust, *J. Geophys. Res.*, *109*, B05407, doi:10.1029/2003JB002744.

Elvevold, S., H. Reginiussen, E. J. Krogh, and F. Bjørklund (1994), Reworking of deep-seated gabbros and associated contact metamorphosed paragneisses in the south-eastern part of the Seiland Igneous Province, northern Norway, *J. Metamorph. Geol.*, *12*, 539–556, doi:10.1111/j.1525-1314.1994.tb00041.x.

Fitz Gerald, J. D., and H. Stünitz (1993), Deformation of granitoids at low metamorphic grade. I: Reactions and grain size reduction, *Tectonophysics*, *221*, 269–297, doi:10.1016/0040-1951(93)90163-E.

Fukuda, J., and T. Okudaira (2013), Grain-size-sensitive creep of plagioclase accompanied by solution-precipitation and mass transfer under midcrustal conditions, *J. Struct. Geol.*, *51*, 61–73, doi:10.1016/j.jsg.2013.03.006.

Fukuda, J., T. Okudaira, T. Satsukawa, and K. Michibayashi (2012), Solution-precipitation of K-feldspar in deformed granitoids and its relationship to the distribution of water, *Tectonophysics*, *532–535*, 175–185, doi:10.1016/0040-1951(93)90163-E.

Fusseis, F., K. Regenauer-Lieb, J. Liu, R. M. Hough, and F. De Carlo (2009), Creep cavitation can establish a dynamic granular fluid pump in ductile shear zones, *Nature*, *459*, 974–977, doi:10.1038/nature08051.

Getsinger, A. J., and G. Hirth (2014), Amphibole fabric formation during diffusion creep and the rheology of shear zones, *Geology*, *42*, 535–538, doi:10.1130/G35327.1.

Getsinger, A. J., G. Hirth, H. Stünitz, and E. T. Goergen (2013), Influence of water on rheology and strain localization in the lower continental crust, *Geochem. Geophys. Geosyst.*, *14*, 2247–2264, doi:10.1002/ggge.20148.

Grove, T. L., M. B. Baker, and R. J. Kinzier (1984), Coupled CaAl-NaSi diffusion in plagioclase feldspar: Experiments and applications to cooling rate speedometry, *Geochim. Cosmochim. Acta*, *48*, 2113–2121, doi:10.1016/0016-7037(84)90391-0.

Hadizadeh, J., and J. Tullis (1992), Cataclastic flow and semibrittle deformation of anorthite, *J. Struct. Geol.*, *14*, 57–63, doi:10.1016/0191-8141(92)90144-L.

Hielscher, R., and H. Schaeben (2008), A novel pole figure inversion method: Specification of the *MTEX* algorithm, *J. Appl. Crystallogr.*, *41*, 1024–1037, doi:10.1107/S0021889808030112.

Holland, T. J. B., and R. Powell (1998), An internally consistent thermodynamic data set for phases petrological interest, *J. Metamorph. Geol.*, *16*, 309–343, doi:10.1111/j.1525-1314.1998.00140.x.

Holland, T., and J. Blundy (1994), Non-ideal interactions in calcic amphiboles and their bearing on amphibole-plagioclase thermometry, *Contrib. Mineral. Petrol.*, *116*, 433–447, doi:10.1007/BF00310910.

Holland, T., and R. Powell (1996), Thermodynamics of order-disorder in minerals. 2. Symmetric formalism applied to solid solution, *Am. Mineral.*, *81*, 1425–1437.

Holland, T., J. Baker, and R. Powell (1998), Mixing properties and activity-composition relationships of chlorites in the system MgO-FeO-Al_2O_3-SiO_2-H_2O, *Eur. J. Mineral.*, *10*, 395–406.

Imon, R., T. Okudaira, and A. Fujimoto (2002), Dissolution and precipitation processes in deformed amphibolites: An example from the ductile shear zone of the Ryoke metamorphic belt, SW Japan, *J. Metamorph. Geol.*, *20*, 297–308, doi:10.1046/j.1525-1314.2002.00367.x.

Imon, R., T. Okudaira, and K. Kanagawa (2004), Development of shape-and lattice-preferred orientations of amphibole grains during initial cataclastic deformation and subsequent deformation by dissolution-precipitation creep in amphibolites from the Ryoke metamorphic belt, SW Japan, *J. Struct. Geol.*, *26*, 793–805, doi:10.1016/j.jsg.2003.09.004.

Jackson, J. (2002), Faulting, flow, and the strength of the continental lithosphere, *Int. Geol. Rev.*, *44*, 39–62, doi:10.2747/0020-6814.44.1.39.

Joesten, R. L. (1991), Kinetics of coarsening and diffusion-controlled mineral growth, in *Contact Metamorphism*, *Rev. Mineral.*, vol. 26, edited by D. M. Kerrick, pp. 507–582.

Kanagawa, K., H. Shimano, and Y. Hiroi (2008), Mylonitic deformation of gabbro in the lower crust: A case study from the Pankenushi gabbro in the Hidaka metamorphic belt of central Hokkaido, Japan, *J. Struct. Geol.*, *30*, 1150–1166, doi:10.1016/j.jsg.2008.05.007.

Keulen, N., R. Heilbronner, H. Stünitz, A.-M. Boullier, and H. Ito (2007), Grain size distributions of fault rocks: A comparison between experimentally and naturally deformed granitoids, *J. Struct. Geol.*, *29*, 1282–1300, doi:10.1016/j.jsg.2007.04.003.

Kohlstedt, D. L., and J. B. Vander Sande (1973), Transmission electron microscopy investigation of the defect microstructure of four natural orthopyroxenes, *Contrib. Mineral. Petrol.*, *42*, 169–180, doi:10.1007/BF00371506.

Kohlstedt, D. L., B. Evans, and S. J. Mackwell (1995), Strength of the lithosphere: Constraints by laboratory experiments, *J. Geophys. Res.*, *100*, 17,587–17,602, doi:10.1029/95JB01460.

Kretz, R. (1983), Symbols for rock-forming minerals, *Am. Mineral.*, *68*, 277–279.

Kronenberg, A. K., and J. Tullis (1984), Flow strength of quartz aggregates: Grain size and pressure effects due to hydrolytic weakening, *J. Geophys. Res.*, *89*, 4281–4297, doi:10.1029/JB089iB06p04281.

Kruse, R., H. Stünitz, and K. Kunze (2001), Dynamic recrystallization processes in plagioclase porphyroclasts, *J. Struct. Geol.*, *23*, 1781–1802, doi:10.1016/S0191-8141(01)00030-X.

Leake, B. E., et al. (1997), Nomenclature of amphiboles: Report of the subcommittee on amphiboles in the International Mineralogical Association, Commission on new minerals and mineral names, *Can. Mineral.*, *35*, 219–246.

Maggi, A., J. A. Jackson, D. McKenzie, and K. Priestley (2000), Earthquake focal depths, effective elastic thickness, and the strength of the continental lithosphere, *Geology*, *28*, 495–498, doi:10.1130/0091-7613(2000)28<495:EFDEET>2.0.CO;2.

Mauler, A., M. Bystricky, K. Kunze, and S. Mackwell (2000), Microstructures and lattice preferred orientations in experimentally deformed clinopyroxene aggregates, *J. Struct. Geol.*, *22*, 1633–1648, doi:10.1016/S0191-8141(00)00073-0.

McLaren, A. C., and L. L. Pryer (2001), Microstructural investigation of the interaction and interdependence of cataclastic and plastic mechanisms in feldspar crystals deformed in the semibrittle field, *Tectonophysics*, *335*, 1–15, doi:10.1016/S0040-1951(01)00042-7.

Menegon, L., H. Stünitz, P. Nasipuri, R. Heilbronner, and H. Svahnberg (2013), Transition from fracturing to viscous flow in granulite facies perthitic feldspar (Lofoten, Norway), *J. Struct. Geol.*, *48*, 95–112, doi:10.1016/j.jsg.2012.12.004.

Miyazaki, K. (1991), Ostwald ripening of garnet in high *P/T* metamorphic rocks, *Contrib. Mineral. Petrol.*, *108*, 118–128, doi:10.1007/BF00307331.

Negrini, M., H. Stünitz, P. Nasipuri, L. Menegon, and L. F. G. Morales (2014), Semibrittle deformation and partial melting of perthitic K-feldspar: An experimental study, *J. Geophys. Res. Solid Earth*, *119*, 3478–3502, doi:10.1002/2013JB010573.

Newton, R. C., T. V. Charlu, and O. J. Kleppa (1980), Thermochemistry of the high structural state plagioclases, *Geochim. Cosmochim. Acta*, *44*, 933–941, doi:10.1016/0016-7037(80)90283-5.

Offerhaus, L. J., R. Wirth, and G. Dresen (2001), High-temperature creep of polycrystalline albite, in *Deformation Mechanisms, Rheology and Tectonics*, edited by S. de Meer et al., pp. 124, Utrecht Univ., Noordwijkerhout, Netherlands.
Parsons, I., J. D. Fitz Gerald, J. K. W. Lee, T. Ivanic, and U. Golla-Schindler (2010), Time-temperature evolution of microtextures and contained fluids in a plutonic alkali feldspar during heating, *Contrib. Mineral. Petrol.*, *160*, 155–180, doi:10.1007/s00410-009-0471-9.
Pec, M., H. Stünitz, and R. Heilbronner (2012), Semi-brittle deformation of granitoid gouges in shear experiments at elevated pressures and temperatures, *J. Struct. Geol.*, *38*, 200–221, doi:10.1016/j.jsg.2011.09.001.
Pedersen, R. B., G. R. Dunning, and B. Robins (1989), U-Pb ages of nepheline syenite pegmatites from the Seiland Magmatic Province, N. Norway, in *The Caledonide Geology of Scandinavia*, edited by R. A. Gayer, pp. 3–8, Graham and Trotman, London, U. K.
Platt, J. P., and W. M. Behr (2011), Lithospheric shear zones as constant stress experiments, *Geology*, *39*, 127–130, doi:10.1130/G31561.1.
Prior, D. J., and J. Wheeler (1999), Feldspar fabrics in a greenschist facies albite-rich mylonite from electron backscatter diffraction, *Tectonophysics*, *303*, 29–49, doi:10.1016/S0040-1951(98)00257-1.
Raimbourg, H., T. Toyoshima, Y. Harima, and G. Kimura (2008), Grain-size reduction mechanisms and rheological consequences in high-temperature gabbro mylonites of Hidaka, Japan, *Earth Planet. Sci. Lett.*, *267*, 637–653, doi:10.1016/j.epsl.2007.12.012.
Roberts, R. J., F. Corfu, T. H. Torsvik, L. D. Ashwal, and D. M. Ramsay (2006), Short-lived mafic magmatism at 570 Ma in the northern Norwegian Caledonides: U-Pb zircon ages from the Seiland Igneous Province, *Geol. Mag.*, *143*, 887–903, doi:10.1017/S0016756806002512.
Robins, B., and P. Gardner (1975), The magmatic evolution of the Seiland province, and Caledonian plate boundaries in Northern Norway, *Earth Planet. Sci. Lett.*, *26*, 167–178, doi:10.1016/0012-821X(75)90084-9.
Ross, J. V., and K. C. Nielsen (1978), High-temperature flow of wet polycrystalline enstatite, *Tectonophysics*, *44*, 233–261, doi:10.1016/0040-1951(78)90072-0.
Rutter, E. H. (1999), On the relationship between the formation of shear zones and the form of the flow law for rocks undergoing dynamic recrystallization, *Tectonophysics*, *303*, 147–158, doi:10.1016/0012-821X(75)90084-9.
Rybacki, E., and G. Dresen (2000), Dislocation and diffusion creep of synthetic anorthite aggregates, *J. Geophys. Res.*, *105*, 26,017–26,036, doi:10.1029/2000JB900223.
Rybacki, E., and G. Dresen (2004), Deformation mechanism maps for feldspar rocks, *Tectonophysics*, *382*, 173–187, doi:10.1016/j.tecto.2004.01.006.
Rybacki, E., R. Wirth, and G. Dresen (2008), High-strain creep of feldspar rocks: Implications for cavitation and ductile failure in the lower crust, *Geophys. Res. Lett.*, *35*, L04304, doi:10.1029/2007GL032478.
Sammis, C. G., R. Osborne, J. L. Anderson, M. Banerdt, and P. White (1986), Self-similar cataclasis in the formation of fault gouge, *Pure Appl. Geophys.*, *124*, 53–78, doi:10.1007/BF00875719.
Sautter, V., O. Jaoul, and F. Abel (1988), Aluminum diffusion in diopside using the $^{27}Al(\rho, \gamma)^{28}Si$ nuclear reaction: Preliminary results, *Earth Planet. Sci. Lett.*, *89*, 109–114, doi:10.1016/0012-821X(88)90036-2.
Scholz, C. H. (1989), Mechanics of faulting, *Ann. Rev. Earth Planet. Sci.*, *17*, 309–334.
Skemer, P., and S.-i. Karato (2007), Effects of solute segregation on the grain-growth kinetics of orthopyroxene with implications for the deformation of the upper mantle, *Phys. Earth Planet. Inter.*, *164*, 186–196, doi:10.1016/j.pepi.2007.06.011.
Steuten, J. M., and H. L. M. van Roermund (1989), An optical and electron microscopy study of defect microstructures in naturally deformed orthopyroxene, *Tectonophysics*, *157*, 331–338, doi:10.1016/0040-1951(89)90148-0.
Stünitz, H. (1998), Syndeformational recrystallization – dynamic or compositionally induces?, *Contrib. Mineral. Petrol.*, *131*, 219–236, doi:10.1007/s004100050390.
Stünitz, H., and J. D. Fitz Gerald (1993), Deformation of granitoids at low metamorphic grade. II: Granular flow in albite-rich mylonites, *Tectonophysics*, *221*, 299–324, doi:10.1016/0040-1951(93)90164-F.
Stünitz, H., and J. Tullis (2001), Weakening and strain localization produced by syn-deformational reaction of plagioclase, *Int. J. Earth Sci.*, *90*, 136–148, doi:10.1007/s005310000148.
Stünitz, H., J. D. Fitz Gerald, and J. Tullis (2003), Dislocation generation, slip systems, and dynamic recrystallization in experimentally deformed plagioclase single crystals, *Tectonophysics*, *372*, 215–233, doi:10.1016/S0040-1951(03)00241-5.
Tegner, C., B. Robins, H. Reginiussen, and S. Grundvig (1999), Assimilation of crustal xenoliths in a basaltic magma chamber: Sr and Nd isotopic constraints from the Hasvik layered intrusion, Norway, *J. Petrol.*, *40*, 363–380, doi:10.1093/petrology/40.3.363.
Thomas, A. M., R. M. Nadeau, and R. Bürgmann (2009), Tremor-tide correlations and near-lithostatic pore pressure on the deep San Andreas fault, *Nature*, *462*, 1048–1051, doi:10.1038/nature08654.
Trepmann, C. A., and B. Stöckhert (2003), Quartz microstructures developed during nonsteady state plastic flow at rapidly decaying stress and strain rate, *J. Struct. Geol.*, *25*, 2035–2051, doi:10.1016/S0191-8141(03)00073-7.
Trepmann, C. A., B. Stöckhert, D. Dorner, R. H. Maghadam, M. Küster, and K. Röller (2007), Simulating coseismic deformation of quartz in the middle crust and fabric evolution during postseismic stress relaxation: An experimental study, *Tectonophysics*, *442*, 83–104, doi:10.1016/j.tecto.2007.05.005.
Tullis, J., and R. A. Yund (1987), Transition from cataclastic flow to dislocation creep of feldspar: Mechanisms and microstructures, *Geology*, *15*, 606–609, doi:10.1130/0091-7613(1987)15<606:TFCFTD>2.0.CO;2.
Uehara, S.-I., and T. Shimamoto (2004), Gas permeability evolution of cataclasite and fault gouge in triaxial compression and implications for changes in fault zone permeability structure through the earthquake cycle, *Tectonophysics*, *378*, 183–195, doi:10.1016/j.tecto.2003.09.007.
Vernooij, M. G. C., K. Kunze, and B. den Brok (2006), 'Brittle' shear zones in experimentally deformed quartz single crystals, *J. Struct. Geol.*, *28*, 1292–1306, doi:10.1016/j.jsg.2006.03.018.
Walker, F. D. L., M. R. Lee, and I. Parsons (1995), Micropores and micropermeable texture in alkali feldspar: Geochemical and geophysical implications, *Mineral. Mag.*, *59*, 505–534, doi:10.1180/minmag.1995.059.396.12.
Wark, D. A., and E. B. Watson (1998), Grain-scale permeabilities of texturally equilibrated, monomineralic rocks, *Earth Planet. Sci. Lett.*, *164*, 591–605, doi:10.1016/S0012-821X(98)00252-0.
Wintsch, R. P., and K. Yi (2002), Dissolution and replacement creep: A significant deformation mechanism in midcrustal rocks, *J. Struct. Geol.*, *24*, 1179–1193, doi:10.1016/S0191-8141(01)00100-6.
Yoshino, T., and D. Yamazaki (2007), Grain growth kinetics of $CaIrO_3$ perovskite and postperovskite, with implications for rheology of D″ layer, *Earth Planet. Sci. Lett.*, *255*, 485–493, doi:10.1016/j.epsl.2007.01.010.
Yoshino, T., J. D. Price, D. A. Wark, and E. B. Watson (2006), Effect of faceting on pore geometry in texturally equilibrated rocks: Implications for low permeability at low porosity, *Contrib. Mineral. Petrol.*, *152*, 169–186, doi:10.1007/s00410-006-0099-y.
Yund, R. A., and J. Tullis (1991), Compositional changes of minerals associated with dynamic recrystallization, *Contrib. Mineral. Petrol.*, *108*, 346–355, doi:10.1007/BF00285942.
Zoback, M. D., and J. Townend (2001), Implications of hydrostatic pore pressures and high crustal strength for the deformation of intraplate lithosphere, *Tectonophysics*, *336*, 19–30, doi:10.1016/S0040-1951(01)00091-9.